

DAMAGE LOCATION IN MECHANICAL STRUCTURES BY MULTI-OBJECTIVE PATTERN SEARCH

CHRISTIAN GÜNTHER, BENEDIKT HOFMEISTER, CLEMENS HÜBLER, CLEMENS JONSCHER,
JASPER RAGNITZ, JENNY SCHUBERT, AND MARC C. STEINBACH

ABSTRACT. We propose a multi-objective global pattern search algorithm for the task of locating and quantifying damage in flexible mechanical structures. This is achieved by identifying eigenfrequencies and eigenmodes from measurements and matching them against the results of a finite element simulation model, which leads to a nonsmooth nonlinear bi-objective parameter estimation problem. A derivative-free optimization algorithm is required since the problem is nonsmooth and also because complex mechanical simulation models are often solved using commercial black-box software. Moreover, the entire set of non-dominated solutions is of interest to practitioners. Most solution approaches published to date are based on meta-heuristics such as genetic algorithms. The proposed multi-objective pattern-search algorithm provides a mathematically well-founded alternative. It features a novel sorting procedure that reduces the complexity in our context. Test runs on two experimental structures with multiple damage scenarios are used to validate the approach. The results demonstrate that the proposed algorithm yields accurate damage locations and requires moderate computational resources. From the engineer's perspective it represents a promising tool for structural health monitoring.

1. INTRODUCTION

A common task in structural engineering is the updating of finite element (FE) models wherein measurements of the mechanical structure are used to estimate parameters of the simulation model [23, 40]. This is necessary when physical properties and hence model parameters may change over time due to wearout, damage, or other reasons. The present work, in particular, addresses the problem of locating and also quantifying damage in terms of stiffness deviations based on detected changes in eigenfrequencies and mode shapes, which is known as *vibration-based model updating* in structural health monitoring [19].

Mathematically this task leads to a nonsmooth and nonlinear bi-objective least-squares parameter estimation problem. Changes of eigenmodes and eigenfrequencies are treated as separate error measures to obtain more error-tolerant results. These error measures depend on certain damage parameters that influence the stiffness matrix and possibly the inertia matrix of the mechanical structure. As the eigenmodes and eigenfrequencies are solutions of an eigenvalue problem for the FE simulation model, their dependence on the parameters is not only nonsmooth and nonlinear but also expensive to evaluate. Moreover, the entire set of non-dominated solutions (the Pareto front or Pareto frontier) is of interest for assessing the outcome of the model updating problem in practical applications. We propose a multi-objective global pattern search algorithm with novel algorithmic elements to compute large numbers of non-dominated points close to the Pareto front.

Finite element model updating was first proposed in the 1990s, notable early contributors are Friswell and Mottershead [23] as well as Link [39]. Commonly, metaheuristic optimization algorithms are used for model updating [37, 30, 31]. Other approaches make use of local optimization algorithms [44] or a combination of a global and a local optimizer

Date: April 3, 2024.

2020 Mathematics Subject Classification. 70J10, 74R99, 90C26, 90C29, 90C59.

Key words and phrases. Mechanical structures, damage location, parameter identification, multi-objective optimization, pattern search.

[45, 5]. Moreover, previous approaches to model updating are frequently based on convex combinations of the mode shape and eigenfrequency error metrics [46]. However, since there is no natural “best” weighting for a given application problem and an appropriate weighting is hard to guess even for experienced practitioners, a priori choices like equal weights usually yield inadequate results [45]. The proper mathematical tool to deal with this situation is multi-objective optimization [41, 9].

Various algorithmic approaches have been developed for solving specific classes of multi-objective optimization problems. These include the generalization of well-known derivative-based single-objective optimization methods, in particular line search algorithms such as the steepest descent method and the Newton algorithm; see, e.g., [21, 24, 20]. Although derivative-based methods are commonly preferred over derivative-free methods because of their superior performance, this view may change if the goal is to compute an approximation to the entire Pareto front of a given multi-objective optimization problem, as recognized in [3]. It is well-known that methods based on solving parametric families of scalar optimization problems (so-called scalarization approaches; e.g. [14, 33]) are useful for the approximation of the Pareto front. Moreover, in recent years also branch and bound methods have been proposed to obtain approximations (coverages) of the set of Pareto efficient solutions and of the Pareto front; e.g., [42, 16, 17].

Similarly, derivative-free methods are often the preferred choice if a multi-objective optimization problem involves highly expensive objective functions. In [48] a trust region type algorithm is presented for multi-objective optimization problems in which one objective function is significantly more expensive than the remaining ones, though under differentiability assumptions on all involved functions. In the model updating application considered here, all objective functions are expensive and nondifferentiable; hence we cannot employ derivative-based algorithms to approximate the desired Pareto fronts. This situation is common in engineering applications where complex numerical models are considered.

Derivative-free methods are generally classified as deterministic, non-deterministic or hybrid. On the same input, deterministic methods always produce the same output, non-deterministic ones may produce different output in different runs, and hybrid methods combine deterministic and non-deterministic features. Deterministic derivative-free methods for multi-objective optimization (in particular for approximating the entire Pareto front) have attracted much less attention than non-deterministic ones. Some well-known methods of this type are proposed in [10, 9, 18, 2]; some hybrid methods are proposed in [32, 10, 2]. In particular, pattern search (or direct search) approaches as extensions of the classical pattern search play a prominent role in this field; e.g., [28, 50, 12, 1].

Non-deterministic derivative-free methods are often used in engineering because they are comparatively easy to implement and to use. Methods of this type follow a random-number-based approach and are used in evolutionary (population-based) multi-objective optimization; see [9] for a survey on this topic. A particularly prominent example is the multi-objective genetic algorithm NSGA-II [11]. A more recent branch of meta-heuristic multi-objective optimizers includes particle swarm approaches, often referred to as MOPSO; see [8] for a survey. We finally notice that there is a very large body of literature on related non-deterministic methods which, however, are not of primary interest in our context as we prefer a mathematically better founded approach.

In this work we propose a deterministic derivative-free algorithm, based on a pattern search approach, to compute large numbers of non-dominated points close to the Pareto front of the given multi-objective optimization problem. To this end, a novel non-dominated sorting procedure for computing first level and also higher level Pareto fronts (similar to NSGA-II in [11]) will play a key role in our algorithm.

The remainder of the paper is structured as follows. In Section 2 we provide some background information on the application problem. The precise mathematical formulations of

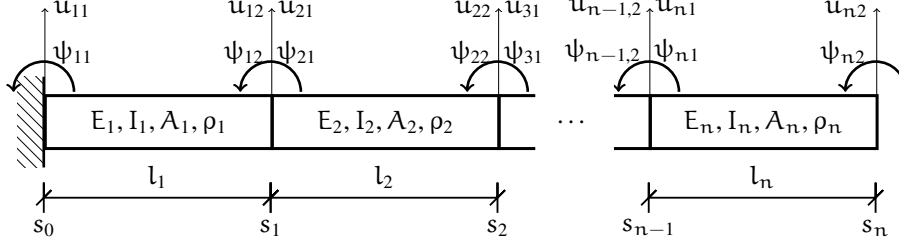
two typical FE simulation models, of our damage model and of the resulting bi-objective optimization problem are presented in Section 3. In Section 4 we describe and discuss the details of our proposed multi-objective global pattern search algorithm. In Section 5 the algorithm is then tested on two mechanical structures with artificial damage to evaluate and demonstrate its effectiveness. We conclude the article with some final remarks and an outlook in Section 6.

2. APPLICATION PROBLEM

In this section we give some additional information on the model updating application. Mathematical details are provided in the following section. While the basic idea of modifying an FE simulation model to match observed changes of the structural behavior always leads to a parameter estimation problem, there is a wide range of situations where model updating is relevant and a multitude of possibilities how to approach this task. The range of situations regards the types and sizes of structures, the types of possible property changes, failures, or damage, the type and quality of the measured data, and the type and amount of derived results required by the engineer to determine the new model parameters. The possibilities of approaching the task may differ in the parameterization of the FE model, in the choice of objective functions and possibly constraints (thus in the mathematical properties of the optimization problem), and in the choice of the solution algorithm.

As already indicated, we address the problem of locating and quantifying damage in flexible structures. More precisely, we restrict ourselves to structures that can be modeled as ensembles of one-dimensional flexible beams, and we consider two beam types of different complexity, the Euler-Bernoulli beam and the Timoshenko beam. In reality the structures of interest may be very large, such as rotor blades of wind turbines. The practicability and cost of obtaining useful measurements determines which structural properties can be monitored in real life. Since acceleration sensors are small and cheap, and since they can continuously deliver data at high sampling rates, we focus on time series of acceleration measurements as data basis for the desired damage location. There are standard methods to determine eigenfrequencies and associated mode shapes of the structure from this data. In principle, we are thus able to locate any kind of damage that changes the stiffness or the inertia of the structure, by choosing changes of the eigenfrequencies and of the mode shapes as two distinct error measures in the parameter estimation problem. This gives the mentioned nonlinear and nonsmooth bi-objective parameter estimation problem, where the choice of constraints depends on the chosen model parameterization and also on the specific application problem. The proposed multi-objective global pattern-search algorithm is then a suitable choice for solving the problem because the entire Pareto front is of interest for determining the updated model parameters.

A central mathematical aspect deserves further discussion: the parameterization of the FE model. The most straightforward option is to assign one parameter to each individual finite element [37]. As FE models often have hundreds or thousands of elements, this approach leads to an excessive number of parameters and typically to an ill-posed optimization problem [46]. To reduce the number of parameters, a strategy commonly used is the assignment of one parameter to a group of elements supposedly having similar mechanical properties, which are then referred to as substructures or super-elements [35]. The more super-elements are employed, the higher the number of parameters becomes. A different approach, which is motivated by a variation of the properties along the structure, uses a damage distribution. This also leads to a formulation with comparatively few parameters. The distribution functions can take various forms, for example quadratic polynomials [47]. In the present work we employ Gaussian damage distribution functions as suggested in [6] to parameterize the structural stiffness of the FE model.

FIGURE 1. Scheme of a cantilever beam with n finite elements.

3. MATHEMATICAL MODEL

3.1. Structural Model. We focus on slender beam structures, considered as essentially one-dimensional mechanical objects. The mathematical models follow a standard finite element approach. A schematic view of a discretized beam is given in Fig. 1.

For the applications considered later, we need two types of models: the Euler-Bernoulli beam and the Timoshenko beam. We start with the simpler Euler-Bernoulli beam model [22, Chapter 5.4] wherein shear effects and rotational inertia are ignored. The beam of length L is discretized into a sequence of n finite elements (not necessarily of equal length) with node positions $s_i \in [0, L]$, $i \in \mathcal{N} = \{0, \dots, n\}$. The degrees of freedom (DoF) of each beam element $e \in \mathcal{E} = \{1, \dots, n\}$ are located at the two end nodes $e-1, e$, locally indexed as $e1, e2$. Each node has two DoF: a lateral displacement $u_{ei} \in \mathbb{R}$ and a rotation angle $\psi_{ei} \in \mathbb{R}$, $i \in \{1, 2\}$. An approximate displacement of a point $\xi \in [0, l_e]$ on beam element e at time t is calculated with four shape functions $N_{ei}: [0, l_e] \rightarrow \mathbb{R}$ as well as the four DoF:

$$u_e(\xi, t) = [N_{e1}(\xi) \quad N_{e2}(\xi) \quad N_{e3}(\xi) \quad N_{e4}(\xi)] q_e(t), \quad q_e(t) = \begin{pmatrix} u_{e1}(t) \\ \psi_{e1}(t) \\ u_{e2}(t) \\ \psi_{e2}(t) \end{pmatrix}, \quad (1)$$

where the shape functions are defined as

$$\begin{aligned} N_{e1}(\xi) &= \left(1 - 3\frac{\xi^2}{l_e^2} + 2\frac{\xi^3}{l_e^3}\right), & N_{e2}(\xi) &= l_e \left(\frac{\xi}{l_e} - 2\frac{\xi^2}{l_e^2} + \frac{\xi^3}{l_e^3}\right), \\ N_{e3}(\xi) &= \left(3\frac{\xi^2}{l_e^2} - 2\frac{\xi^3}{l_e^3}\right), & N_{e4}(\xi) &= l_e \left(-\frac{\xi^2}{l_e^2} + \frac{\xi^3}{l_e^3}\right). \end{aligned} \quad (2)$$

Here $l_e = s_e - s_{e-1}$ is the length of beam element e , and (1) is a cubic polynomial in ξ .

The stiffness matrix $\mathbf{K}_e \in \mathbb{R}^{4 \times 4}$ and the mass matrix $\mathbf{M}_e \in \mathbb{R}^{4 \times 4}$ of beam element e are derived from (approximations of) the strain energy U_e and the kinetic energy T_e . Under the assumptions of a linear elastic material and a constant area moment of inertia I_e (also called second moment of area), the strain energy is approximated as

$$U_e(t) = \frac{1}{2} E_e I_e \int_0^{l_e} u_e''(\xi, t)^2 d\xi,$$

where E_e is Young's modulus and u_e' denotes the partial derivative with respect to ξ . The area moment of inertia is

$$I_e = \frac{w_e t_e^3}{12},$$

where w_e is the width of the rectangular beam cross section and t_e is its thickness [49, Appendix A.1]. Together with (1) we obtain

$$U_e(t) = \frac{1}{2} q_e(t)^T \mathbf{K}_e q_e(t),$$

This dependence is assumed to be caused by a dependence of each Young's modulus on x , with details given in Section 3.2,

$$\mathbf{K}_e(x) = \frac{E_e(x)I_e}{l_e^3} \begin{bmatrix} 12 & 6l_e & -12 & 6l_e \\ 6l_e & 4l_e^2 & -6l_e & 2l_e^2 \\ -12 & -6l_e & 12 & -6l_e \\ 6l_e & 2l_e^2 & -6l_e & 4l_e^2 \end{bmatrix}. \quad (5)$$

To account for shear effects and rotational inertia, we now introduce the extended model of a Timoshenko beam [22, Chapter 5.4]. There are approaches that increase the DoF per node to account for shear. However, we follow a reduced integration approach to retain only two DoF per node: the lateral displacement u_e and the angle of the beam cross section ψ_e . The angle of the beam cross section is given as

$$\psi_e(\xi, t) = u_e'(\xi, t) + \beta_e(\xi, t).$$

Herein β_e denotes the shear angle,

$$\beta_e(\xi, t) = \frac{\Phi_e l_e^2}{12} u_e'''(\xi, t), \quad \Phi_e = \frac{12E_e I_e}{\kappa_e G_e A_e l_e^2}, \quad (6)$$

where κ_e is the shear constant (which depends on the shape of the cross section) and G_e is the shear modulus. Similar to the Euler-Bernoulli beam, we obtain

$$u_e(\xi, t) = [N_{e1}(\xi) \quad N_{e2}(\xi) \quad N_{e3}(\xi) \quad N_{e4}(\xi)] q_e(t), \quad (7)$$

where q_e is defined as in (1) and the shape functions are now defined as

$$\begin{aligned} N_{e1}(\xi) &= \frac{1}{1 + \Phi_e} \left(1 + \Phi_e - \Phi_e \frac{\xi}{l_e} - 3 \frac{\xi^2}{l_e^2} + 2 \frac{\xi^3}{l_e^3} \right), \\ N_{e2}(\xi) &= \frac{l_e}{1 + \Phi_e} \left(\frac{2 + \Phi_e}{2} \frac{\xi}{l_e} - \frac{4 + \Phi_e}{2} \frac{\xi^2}{l_e^2} + \frac{\xi^3}{l_e^3} \right), \\ N_{e3}(\xi) &= \frac{1}{1 + \Phi_e} \left(\Phi_e \frac{\xi}{l_e} + 3 \frac{\xi^2}{l_e^2} - 2 \frac{\xi^3}{l_e^3} \right), \\ N_{e4}(\xi) &= \frac{l_e}{1 + \Phi_e} \left(-\frac{\Phi_e}{2} \frac{\xi}{l_e} - \frac{2 - \Phi_e}{2} \frac{\xi^2}{l_e^2} + \frac{\xi^3}{l_e^3} \right). \end{aligned} \quad (8)$$

If $\Phi_e = 0$, shear effects are neglected and the shape functions (8) are identical to (2). The strain energy for the element, including shear, is

$$U_e = \frac{1}{2} E_e \int_0^{l_e} I_e(\xi) \psi_e'(\xi, t)^2 d\xi + \frac{1}{2} \kappa_e G_e \int_0^{l_e} A_e(\xi) \beta_e(\xi, t)^2 d\xi.$$

For a constant element cross section we have

$$\psi_e'(\xi, t) = u_e''(\xi, t) + \beta_e'(\xi, t) = u_e''(\xi, t),$$

because β_e is constant along the element. Thus, the approximate strain energy is

$$U_e(t) = \frac{1}{2} q_e(t)^T \mathbf{K}_e q_e(t),$$

with the elements of the stiffness matrix being

$$k_{e,ij} = E_e I_e \int_0^{l_e} N_{ei}''(\xi) N_{ej}''(\xi) d\xi + \frac{E_e I_e \Phi_e l_e^2}{12} \int_0^{l_e} N_{ei}'''(\xi) N_{ej}'''(\xi) d\xi.$$

This gives the stiffness matrix

$$\mathbf{K}_e = \frac{E_e I_e}{(1 + \Phi_e) l_e^3} \begin{bmatrix} 12 & 6l_e & -12 & 6l_e \\ 6l_e & l_e^2(4 + \Phi_e) & -6l_e & l_e^2(2 - \Phi_e) \\ -12 & -6l_e & 12 & -6l_e \\ 6l_e & l_e^2(2 - \Phi_e) & -6l_e & l_e^2(4 + \Phi_e) \end{bmatrix}. \quad (9)$$

The kinetic energy is

$$\begin{aligned} T_e &= \frac{1}{2} \int_0^{l_e} (\rho_e A_e(\xi) \dot{u}_e(\xi, t)^2 + \rho_e I_e \dot{\psi}_e(\xi, t)^2) d\xi \\ &= \frac{1}{2} \int_0^{l_e} (\rho_e A_e(\xi) \dot{u}_e(\xi, t)^2 + \rho_e I_e [\dot{\beta}_e(\xi, t) + \dot{u}'_e(\xi, t)]^2) d\xi. \end{aligned}$$

Again we write the approximate kinetic energy as

$$T_e(t) = \frac{1}{2} \dot{q}_e(t)^T \mathbf{M}_e \dot{q}_e(t),$$

where the elements of the mass matrix are now

$$\begin{aligned} m_{e,ij} &= \rho_e A_e \int_0^{l_e} N_{ei}(\xi) N_{ej}(\xi) d\xi + \\ &\rho_e I_e \int_0^{l_e} \left(\frac{\Phi_e l_e^2}{12} N_{ei}'''(\xi) + N'_{ei}(\xi) \right) \left(\frac{\Phi_e l_e^2}{12} N_{ej}'''(\xi) + N'_{ej}(\xi) \right) d\xi. \end{aligned}$$

Both integrals can be evaluated analytically, yielding

$$\begin{aligned} \mathbf{M}_e &= \frac{\rho_e A_e l_e}{840(1 + \Phi_e)^2} \begin{bmatrix} m_1 & m_2 & m_3 & m_4 \\ m_2 & m_5 & -m_4 & m_6 \\ m_3 & -m_4 & m_1 & -m_2 \\ m_4 & m_6 & -m_2 & m_5 \end{bmatrix} + \\ &\frac{\rho_e I_e}{30(1 + \Phi_e)^2 l_e} \begin{bmatrix} m_7 & m_8 & -m_7 & m_8 \\ m_8 & m_9 & -m_8 & m_{10} \\ -m_7 & -m_8 & m_7 & -m_8 \\ m_8 & m_{10} & -m_8 & m_9 \end{bmatrix}, \end{aligned} \quad (10)$$

where

$$\begin{aligned} m_1 &= 312 + 588\Phi_e + 280\Phi_e^2, & m_6 &= -(6 + 14\Phi_e + 7\Phi_e^2)l_e^2, \\ m_2 &= (44 + 77\Phi_e + 35\Phi_e^2)l_e, & m_7 &= 36, \\ m_3 &= 108 + 252\Phi_e + 140\Phi_e^2, & m_8 &= (3 - 15\Phi_e)l_e, \\ m_4 &= -(26 + 63\Phi_e + 35\Phi_e^2)l_e, & m_9 &= (4 + 5\Phi_e + 10\Phi_e^2)l_e^2, \\ m_5 &= (8 + 14\Phi_e + 7\Phi_e^2)l_e^2, & m_{10} &= (-1 - 5\Phi_e + 5\Phi_e^2)l_e^2. \end{aligned}$$

The second matrix represents the effect of rotational inertia. If shear effects and rotational inertia are ignored, (10) reduces to the Euler-Bernoulli mass matrix.

The mass matrix and stiffness matrix of the entire beam are assembled in the same way as before, and all mass matrices and stiffness matrices are symmetric positive definite.

Note that the Young's modulus E_e now appears not only in the stiffness matrix but via Φ_e from (6) also in the mass matrix. Thus all these quantities may depend on the damage parameter vector \mathbf{x} : $E_e(\mathbf{x})$, $\Phi_e(\mathbf{x})$, $\mathbf{K}_e(\mathbf{x})$, $\mathbf{M}_e(\mathbf{x})$, and finally $\mathbf{K}(\mathbf{x})$ and $\mathbf{M}(\mathbf{x})$.

3.2. Damage Model. To model the damage we choose a univariate Gaussian distribution described by three parameters $\mathbf{x} \in \mathbb{R}^3$,

$$\Delta(s; \mathbf{x}) = \frac{D}{\sigma\sqrt{2\pi}} \exp\left(-\frac{(s - \mu)^2}{2\sigma^2}\right), \quad \mathbf{x} = (D, \mu, \sigma).$$

Here D is the damage severity (the total weight of the distribution), μ is the center of the damage location, and σ is the standard deviation of the damage distribution, a measure of the damage extent, see Fig. 2. In earlier work [52], we have also experimented with uniform distributions as damage models, and the Gaussian distributions appear to be the better match for most scenarios. The parameters of primary interest in typical structural health monitoring situations are the location μ and the severity D since the goal is to detect and locate small damage scenarios. The extent σ is basically a technical parameter which,

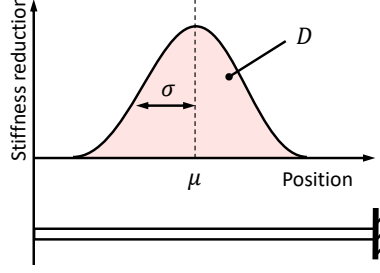


FIGURE 2. Damage distribution function.

however, provides information on the accuracy of the location. The severity has been chosen as the total weight rather than the maximal value of Δ , i.e., $D/(\sigma\sqrt{2\pi})$, because this reduces the sensitivity of the model response (eigenvalues and eigenfunctions) with respect to the less relevant parameter σ .

The damage distribution function is used to scale the initial stiffness of each beam element e . This is accomplished by a scaling factor $\theta_e(\mathbf{x})$ that enters into (5) and similarly into (9) and via (6) into (10),

$$E_e(\mathbf{x}) = \theta_e(\mathbf{x})E_e^0, \quad (11)$$

where E_e^0 is Young's modulus of beam element e in the undamaged state.

Note that it is also possible to set up a more detailed model with stiffness values for axial, shear, bending and torsional strains, each depending individually on the damage. However, such a model would yield an excessive number of damage parameters that could not be determined efficiently in practice.

The scaling factors $\theta_e(\mathbf{x})$ are calculated using the cumulative distribution function F associated with Δ ,

$$F(s; \mathbf{x}) = \int_{-\infty}^s \Delta(r; \mathbf{x}) \, dr.$$

where s is taken as a node position along the structure. Following this approach, the stiffness scaling factors θ_e are defined as

$$\theta_e(\mathbf{x}) = 1 - L \frac{F(s_e; \mathbf{x}) - F(s_{e-1}; \mathbf{x})}{l_e}. \quad (12)$$

This results in a uniform distribution of the damage on each element. In other words, it converts the smooth distribution Δ (truncated to $[0, L]$) into an element-wise constant distribution with the same weight, $\int_0^L \Delta(r; \mathbf{x}) \, dr \approx D$.

3.3. Optimization Model. The damage location problem has the basic structure of a nonlinear inequality-constrained bi-objective optimization problem,

$$\min_{\mathbf{x} \in \mathbb{R}^3} f(\mathbf{x}) \quad \text{s.t.} \quad \mathbf{x} \in [\mathbf{x}^-, \mathbf{x}^+], \quad c_e(\mathbf{x}) \geq 0, \quad e \in \mathcal{E}. \quad (13)$$

Here both components of f are least-squares error measures, see Section 3.3.2, and in addition to component-wise lower and upper bounds \mathbf{x}^- and \mathbf{x}^+ we have a nonlinear constraint at each element $e \in \mathcal{E}$. The functions $c_e: \mathbb{R}^3 \rightarrow \mathbb{R}$ are smooth whereas $f: \mathbb{R}^3 \rightarrow \mathbb{R}^2$ is not differentiable as it involves eigenvalues of the mechanical structure which merely depend continuously on the parameter vector \mathbf{x} . We therefore combine the nonlinear constraints into a single equivalent constraint,

$$c(\mathbf{x}) := \min_{e \in \mathcal{E}} c_e(\mathbf{x}) \geq 0, \quad (14)$$

which introduces artificial nonsmoothness but does not destroy any structure that our pattern search algorithm could otherwise exploit. In fact, although pattern search algorithms

cannot handle nonlinear equality constraints well, nonlinear inequalities are properly incorporated via infinite penalties at infeasible points [7]. Thus, we finally replace (13) with

$$\min_{\mathbf{x} \in \mathbb{R}^3} \bar{f}(\mathbf{x}) \quad \text{s.t.} \quad \mathbf{x} \in [\mathbf{x}^-, \mathbf{x}^+], \quad \bar{f}(\mathbf{x}) = \begin{cases} f(\mathbf{x}), & c(\mathbf{x}) \geq 0, \\ (+\infty), & c(\mathbf{x}) < 0. \end{cases} \quad (15)$$

The specific bounds in our case are chosen as follows:

- $\mu \in [0, L]$: the damage center is on the structure;
- $\sigma \in [0, L]$: the damage extent is in a reasonable range;
- $D \in [0, D_{\max}]$ with $D_{\max} \leq 1$: the damage severity is in a reasonable range.

The upper bound L on σ is artificial. Since lower and upper bounds are required to define the search area of our pattern search algorithm, we choose a relatively large value to reduce the risk of missing any optima. The choice of D_{\max} is problem-specific: if the damage is already known to be smaller, a value $D_{\max} < 1$ reduces the range that is to be searched by the algorithm. The value $D_{\max} = 1$ corresponds to a “full” damage that extends over all beam elements: then σ is at its upper bound and all stiffness factors θ_e are close to zero. This extreme case is very unlikely in practice where both D and σ are typically small.

The specific nonlinear constraints enforce positive values of the stiffness scaling factors,

$$c_e(\mathbf{x}) := \theta_e(\mathbf{x}) - \theta_{\min} \quad \text{where} \quad \theta_{\min} > 0. \quad (16)$$

Positivity is not guaranteed by (12), and in fact $\theta_e(\mathbf{x})$ can become negative for small values of σ , which in turn may lead to an indefinite stiffness matrix $\mathbf{K}(\mathbf{x})$. The exact choice of θ_{\min} is application-specific.

In realistic cases the box constraints remain usually inactive, with the exceptions of $D = 0$ (no damage) and $\mu = 0$ or $\mu = L$ (damage at an end of the structure). As to the nonlinear constraint (14), we observe no significant influence on the optimal solutions for the relatively mild damage cases regarded in this work. It rather becomes relevant only at the initial iterations of our optimization algorithm, when the sampling pattern is not yet focused close to a global optimum. However, the constraint appears to help guiding the algorithm away from unreasonable areas in the damage parameter space and, thus, aids in increasing the convergence speed.

3.3.1. Eigenvalue Problem. We assume that an external excitation $\mathbf{p}(t)$ of the mechanical structure generates only a small deviation $\mathbf{u}(t)$ from some equilibrium state, so that a standard linearly elastic damped oscillation appropriately describes the dynamics,

$$\mathbf{M}(\mathbf{x})\ddot{\mathbf{u}}(t) + \mathbf{B}\dot{\mathbf{u}}(t) + \mathbf{K}(\mathbf{x})\mathbf{u}(t) = \mathbf{p}(t). \quad (17)$$

The modal parameters of the mechanical model are then obtained from the generalized parameter-dependent eigenvalue problem

$$[\mathbf{K}(\mathbf{x}) - \lambda_k(\mathbf{x})^2 \mathbf{M}(\mathbf{x})]\mathbf{u}_k(\mathbf{x}) = \mathbf{0}. \quad (18)$$

Here $\lambda_k(\mathbf{x})$ are the eigenvalues, and $\mathbf{u}_k(\mathbf{x}) \in \mathbb{R}^N$ are the corresponding eigenvectors, i.e., spatially discretized eigenfunctions, which are called *mode shapes* in the engineering context. The chosen formulation neglects damping and requires that there is no external driving force. Depending on the specific mechanical system, multiple eigenvalues may occur, for instance when considering bending modes of rotationally symmetric structures. The oscillation frequencies corresponding to the eigenvalues are

$$f_k(\mathbf{x}) = \frac{\lambda_k(\mathbf{x})}{2\pi}. \quad (19)$$

It follows from (18) that the eigenvalues λ_k depend continuously on the matrices \mathbf{K} and \mathbf{M} but in general not differentially. Thus, even though $\mathbf{K}(\mathbf{x})$ and $\mathbf{M}(\mathbf{x})$ are smooth, $\lambda_k(\mathbf{x})$ is generally nonsmooth.

TABLE 1. States of the structure considered in model updating.

	Measurement	Simulation
Reference (healthy)	M0	S0
Analysis (damaged)	M1	S1

3.3.2. *Least-Squares Error Measures.* The measured data are time series of acceleration measurements obtained from several sensors that are placed along the structure. The sensor positions correspond to a subset of m components of the mode shapes $\mathbf{u}_k(\mathbf{x})$, which are selected by multiplication with a gather matrix $\mathbf{S} \in \{0, 1\}^{m \times N}$. In addition, a normalization using the ℓ_2 -norm is carried out to obtain

$$\Phi_k(\mathbf{x}) = \frac{\mathbf{S}\mathbf{u}_k(\mathbf{x})}{\|\mathbf{S}\mathbf{u}_k(\mathbf{x})\|} \in \mathbb{R}^m. \quad (20)$$

The normalized mode shapes $\Phi_k(\mathbf{x})$ can be directly compared to the mode shapes identified from measurement data. The identification of mode shapes Φ_k and eigenfrequencies f_k from acceleration measurements is achieved by the Bayesian Operational Modal Analysis (BayOMA) [4].

In the model updating framework, four separate states and associated data sets of the monitored structure are involved. These states are generated by combining measured and simulated systems with reference and analysis states. The reference and analysis states correspond to healthy and damaged structures, respectively. The four combinations are given in Table 1, where the states are labeled with M (measured), S (simulated), 0 (reference) and 1 (analysis). For damage location, the states M0, M1 as well as S0 are constant and only S1 is variable and subject to model updating. The following two types of errors need to be considered when setting up the least-squares objective:

- (1) Modeling errors in the simulation model (epistemic uncertainty) lead to different mechanical properties of measurement and simulation even in the reference state. Although these errors could in principle be reduced by more accurate modeling, a significant mismatch between measurement and simulation remains in practice. We refer to this modeling error in the reference state as “error of order 0”.
- (2) The sensitivities of the real mechanical system and its simulation with respect to damage are roughly equal but not exactly. We refer to this modeling error in the sensitivity with respect to damage as “error of order 1”.

To eliminate the error of order 0 from the mismatch between simulation and measurement, we define the mismatch in terms of the (normalized) differences between the respective damaged and healthy states. Then, using eigenfrequencies as well as mode shapes to utilize the full information contained in these modal parameters, we obtain the objective function $f(\mathbf{x}) = (\varepsilon_f(\mathbf{x}), \varepsilon_m(\mathbf{x}))$ in terms of two least-squares errors:

$$\begin{aligned} \varepsilon_f(\mathbf{x})^2 &= \sum_{k \in \mathcal{M}} \left(\frac{f_{S1,k}(\mathbf{x}) - f_{S0,k}}{f_{S0,k}} - \frac{f_{M1,k} - f_{M0,k}}{f_{M0,k}} \right)^2, \\ \varepsilon_m(\mathbf{x})^2 &= \sum_{k \in \mathcal{M}} \|(\Phi_{S1,k}(\mathbf{x}) - \Phi_{S0,k}) - (\Phi_{M1,k} - \Phi_{M0,k})\|^2. \end{aligned} \quad (21)$$

Here \mathcal{M} is the set of modes taken into consideration, ε_f is the eigenfrequency error and ε_m is the mode shape error. As mentioned, the damage parameters only influence the simulation results of the damaged case S1 while all other terms of (21) are constant. All mode shapes in ε_m are normalized according to (20), similar to the approach of the enhanced COMAC metric [29] which has been proposed for structural monitoring.

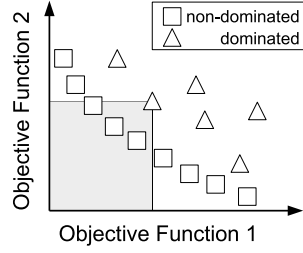


FIGURE 3. Sketch of objective value space in multi-objective optimization and Pareto dominance.

4. OPTIMIZATION ALGORITHM

In this section, we present the Multi-Objective Global Pattern Search Algorithm for approximating solutions to multi-objective optimization problems such as the bi-objective damage location problem given in Section 3.3.

4.1. Multi-objective optimization. Given a vector-valued function

$$f = (f_1, \dots, f_m): \Omega \rightarrow \mathbb{R}^m \cup \{+\infty\}^m$$

with $m \geq 2$ component functions $f_1, \dots, f_m: \Omega \rightarrow \mathbb{R} \cup \{+\infty\}$ and a nonempty feasible set $\Omega \subseteq \mathbb{R}^n$, our general multi-objective optimization problem is given as

$$\begin{cases} f(\mathbf{x}) = (f_1(\mathbf{x}), \dots, f_m(\mathbf{x})) \rightarrow \min, \\ \mathbf{x} \in \Omega. \end{cases} \quad (\text{MOP})$$

A feasible point $\mathbf{x} \in \Omega$ is a Pareto-efficient (Pareto-optimal) solution of the problem (MOP) if there is no $\bar{\mathbf{x}} \in \Omega$ such that

$$\begin{aligned} f_i(\bar{\mathbf{x}}) &\leq f_i(\mathbf{x}) \quad \text{for all } i = 1, \dots, m, \\ f_j(\bar{\mathbf{x}}) &< f_j(\mathbf{x}) \quad \text{for some } j \in \{1, \dots, m\}. \end{aligned}$$

In other words, $\mathbf{x} \in \Omega$ is a Pareto-efficient solution if $f(\mathbf{x}) \notin \{+\infty\}^m$ and

$$f[\Omega] \cap (\{f(\mathbf{x})\} - \mathbb{R}_+^m) = \{f(\mathbf{x})\},$$

where $f[\Omega] := \{f(\bar{\mathbf{x}}) \mid \bar{\mathbf{x}} \in \Omega\}$ is the image of Ω under f and \mathbb{R}_+^m is the nonnegative orthant (the so-called natural ordering cone) in \mathbb{R}^m . The set of Pareto-efficient solutions is denoted by $\text{Eff}(\Omega \mid f)$ and the set of non-dominated image points (the so-called Pareto front or Pareto frontier) is given by $\text{ND}(f[\Omega])$, where

$$\text{ND}(A) := \{a \in A \mid a \notin A \setminus \{a\} + \mathbb{R}_+^m\}$$

for any set $A \subseteq \mathbb{R}^m \cup \{+\infty\}^m$. Obviously, $f[\text{Eff}(\Omega \mid f)] = \text{ND}(f[\Omega])$. The efficiency concept in multi-objective optimization dates back to the works by Edgeworth [13] and Pareto [43]. Some overview on multi-objective optimization can be found in the books by Ehrgott [14] and Jahn [33] or in the survey by Eichfelder [15].

In Fig. 3, the points marked by squares constitute the set of non-dominated image points, while the points marked by triangles are dominated by several other points and are therefore not on the Pareto front.

4.2. Penalty approach for the nonlinear constraints. In many practical problems, such as our model updating problem given in Section 3.3, Ω is given by a set of the type

$$\{\mathbf{x} \in [\mathbf{x}^-, \mathbf{x}^+] \mid c_1(\mathbf{x}) \geq 0, \dots, c_l(\mathbf{x}) \geq 0\}, \quad (22)$$

where $c_1, \dots, c_l: [\mathbf{x}^-, \mathbf{x}^+] \rightarrow \mathbb{R}$, $l \in \mathbb{N}$, are constraint functions, and \mathbf{x}^- and \mathbf{x}^+ are component-wise lower and upper bounds. Penalty methods in multi-objective optimization

aim to transform the problem (MOP) with feasible set given in (22) into a corresponding problem of type (MOP) involving a single box constraint $\mathbf{x} \in [\mathbf{x}^-, \mathbf{x}^+]$. Consider a penalty function $\varphi: [\mathbf{x}^-, \mathbf{x}^+] \rightarrow \mathbb{R}_+ \cup \{+\infty\}$ with the property that for any $\mathbf{x} \in [\mathbf{x}^-, \mathbf{x}^+]$,

$$\varphi(\mathbf{x}) = 0 \iff c_1(\mathbf{x}) \geq 0, \dots, c_l(\mathbf{x}) \geq 0.$$

For instance, in numerical penalty methods the function φ is often defined by

$$\varphi(\mathbf{x}) := -\min\{0, c_1(\mathbf{x}), \dots, c_l(\mathbf{x})\} \quad \text{or by} \quad \varphi(\mathbf{x}) := \sum_{i=1}^l \min\{0, c_i(\mathbf{x})\}^2.$$

For given (sufficiently large) penalty parameters $\alpha_1, \dots, \alpha_m > 0$ we consider the penalized multi-objective optimization problem

$$\begin{cases} (f + \alpha\varphi)(\mathbf{x}) = (f_1(\mathbf{x}) + \alpha_1\varphi(\mathbf{x}), \dots, f_m(\mathbf{x}) + \alpha_m\varphi(\mathbf{x})) \rightarrow \min, \\ \mathbf{x} \in [\mathbf{x}^-, \mathbf{x}^+]. \end{cases} \quad (\text{MOP}_{\text{pen}})$$

In the literature, various relationships are established between the problems (MOP) and (MOP_{pen}); see, e.g., Ye [53] and Günther et al. [25]. From a theoretical point of view, one can also apply the method of infinite penalty (extreme barrier approach), which is based on

$$\varphi(\mathbf{x}) := \begin{cases} 0 & \text{for } \min\{c_1(\mathbf{x}), \dots, c_l(\mathbf{x})\} \geq 0, \\ +\infty & \text{otherwise,} \end{cases}$$

and $\alpha_1 = \dots = \alpha_m = 1$.

Based on the above considerations, in the following sections we consider the problem (MOP) with a feasible set Ω given by a single box constraint, $\Omega := [\mathbf{x}^-, \mathbf{x}^+]$, and we employ the method of infinite penalty.

4.3. Basic ideas of the pattern search approach. In our pattern search approach, we create a pattern as usual (for such a type of algorithm) by performing a one-at-a-time permutation around a base vector $\mathbf{b} = (\mathbf{b}_1, \dots, \mathbf{b}_n)$ using a step width vector $\mathbf{w} = (\mathbf{w}_1, \dots, \mathbf{w}_n)$. New pattern sampling points are then defined for each $i = 1, \dots, n$ by the vectors

$$s_i^-(\mathbf{b}) := \mathbf{b} - \mathbf{w}_i e^i \quad \text{and} \quad s_i^+(\mathbf{b}) := \mathbf{b} + \mathbf{w}_i e^i,$$

where e^i is the i -th canonical basis vector in \mathbb{R}^n . To represent the resulting grid in floating-point arithmetic, we need to avoid unnecessary rounding errors. For instance, the equality $\mathbf{b}^1 + \mathbf{w}_i e^i = \mathbf{b}^2 - \mathbf{w}_i e^i$ with base vectors \mathbf{b}^1 and \mathbf{b}^2 might hold in exact arithmetic but not in floating-point arithmetic. For this reason, we introduce the box $[0, 2^N]^n$ and basis vectors with integer coordinates to obtain the following transformed multi-objective optimization problem:

$$\begin{cases} g(s) = (f_1(h(s)), \dots, f_m(h(s))) \rightarrow \min \\ s \in [0, 2^N]^n. \end{cases} \quad (\text{MOP}_g)$$

Here $h: [0, 2^N]^n \rightarrow [\mathbf{x}^-, \mathbf{x}^+]$ is a bijective linear function defined as

$$h_i(s) := \mathbf{x}_i^- + 2^{-N} s_i (\mathbf{x}_i^+ - \mathbf{x}_i^-) \quad \text{for all } s = (s_1, \dots, s_n) \in [0, 2^N]^n, \quad i = 1, \dots, n,$$

and $g: [0, 2^N]^n \rightarrow \mathbb{R}^m \cup \{+\infty\}^m$ is defined as

$$g(s) := f(h(s)) \quad \text{for all } s \in [0, 2^N]^n.$$

It is easy to check that $f[[\mathbf{x}^-, \mathbf{x}^+]] = g[[0, 2^N]^n]$, and so

$$\text{ND}(f[[\mathbf{x}^-, \mathbf{x}^+]]) = \text{ND}(g[[0, 2^N]^n]).$$

Moreover, using the bijection property of h we get

$$\text{Eff}([\mathbf{x}^-, \mathbf{x}^+] \mid f) = h[\text{Eff}([0, 2^N]^n \mid g)].$$

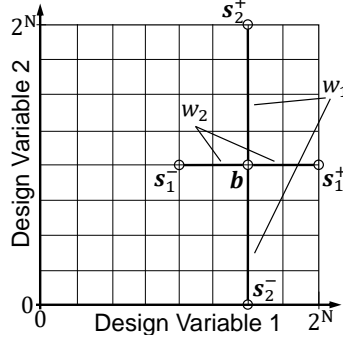


FIGURE 4. Sampling pattern of our Multi-Objective Global Pattern Search Algorithm in two dimensions.

When applying a pattern search scheme to the problem (MOP_g) , the set

$$G_{\mathbb{Z}} := ([0, 2^N] \cap \mathbb{Z})^n,$$

which consists of all integer grid points in the box $[0, 2^N]^n$, is of particular interest. In our approach we will use step widths $w_1, \dots, w_n \in \{2^0, 2^1, \dots, 2^{N-1}\}$, and so if $\mathbf{b} \in G_{\mathbb{Z}}$ and $s_i^-(\mathbf{b}), s_i^+(\mathbf{b}) \in [0, 2^N]^n$, then $s_i^-(\mathbf{b}), s_i^+(\mathbf{b}) \in G_{\mathbb{Z}}$. Roughly speaking, our Multi-Objective Global Pattern Search Algorithm is an iterative procedure based on the following tasks:

- Define a set of base vectors (to start, take the point $\mathbf{b} = 2^{N-1}(1, \dots, 1)$, which is the center of the box $[0, 2^N]^n$, and the step width vector $\mathbf{w} = \mathbf{b}$).
- Sample new points in $G_{\mathbb{Z}}$ (with the aid of $s_i^-(\mathbf{b})$ and $s_i^+(\mathbf{b})$) around all base vectors.
- Apply a non-dominated sorting procedure to all current base vectors and new sampling points to obtain a new set of base vectors for the next iteration.
- Halve the maximum step width of one variable if the set of base vectors does not change in two iterations.

The algorithm stops if the maximum of the step widths is equal to one. By taking a look at the above approach (in particular, the definition of h), one can see that a larger parameter N leads to a larger integer grid $G_{\mathbb{Z}}$ and so to a finer grid in the original box $h[[0, 2^N]^n] = [\mathbf{x}^-, \mathbf{x}^+]$. The integer grid $G_{\mathbb{Z}}$, the pattern generation scheme in the box $[0, 2^N]^n$, and the resulting sampling points $s_1^-(\mathbf{b}), s_1^+(\mathbf{b}), s_2^-(\mathbf{b}), s_2^+(\mathbf{b})$ around a base vector \mathbf{b} are illustrated in Fig. 4 for a two-dimensional example.

The process of identifying the non-dominated set $ND(A)$ of a finite set of points, such as $A = \{a^1, \dots, a^p\} \subseteq f[\Omega] \cup \{+\infty\}^m$, is called non-dominated sorting in the literature [34]. In our Multi-Objective Global Pattern Search Algorithm, we use the Graef-Younes method with presorting (see Günther and Popovici [26], and also Jahn [33, Sec. 12.4]) for the non-dominated sorting phase, which we recall in the following part of the section.

Consider a vector $\lambda = (\lambda_1, \dots, \lambda_m) \in \mathbb{R}^m$, $\lambda_i > 0$ for all $i = 1, \dots, m$, and a function $\varphi_{\lambda}: A \rightarrow \mathbb{R}$ defined by

$$\varphi_{\lambda}(a) := \lambda^T a \quad \text{for all } a \in A.$$

In multi-objective optimization, the strongly \mathbb{R}_+^m -increasing function φ_{λ} is used in the weighted sum (linear) scalarization method (see Jahn [33]). For the given choice of λ one has

$$\arg \min_{a \in A} \varphi_{\lambda}(a) \subseteq ND(A).$$

The Graef-Younes method [33, Sec. 12.4] given in the following Algorithm 1 produces a set $B \subseteq A$ with the property $ND(A) \subseteq B$.

Algorithm 1 Graef-Younes reduction method (function GraefYounesReductionMethod)

```

Input:  $A = \{a^1, \dots, a^p\}$ 
 $B \leftarrow \{a^1\}$ 
for  $k \leftarrow 2$  to  $p$  do
  if  $a^k \notin B + \mathbb{R}_+^m$  then
     $B \leftarrow B \cup \{a^k\}$ 
  end if
end for
Output:  $B \subseteq A$  with  $\text{ND}(A) \subseteq B$ 

```

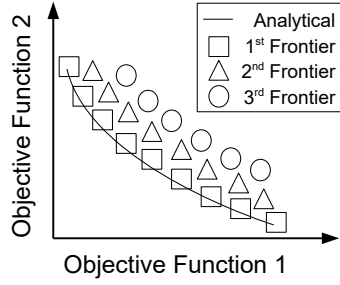


FIGURE 5. Illustration of higher level Pareto fronts resulting from repeated non-dominated sorting.

In our proposed algorithm, we use the Graef-Younes method with presorting to generate the set $B = \text{ND}(A)$, as shown in Algorithm 2 (see Günther and Popovici [26]).

Algorithm 2 Graef-Younes method with presorting procedure

```

Input:  $A = \{a^1, \dots, a^p\}$ 
Compute an enumeration  $A = \{a^{j_1}, \dots, a^{j_p}\}$  such that

$$\varphi_\lambda(a^{j_1}) \leq \varphi_\lambda(a^{j_2}) \leq \dots \leq \varphi_\lambda(a^{j_p}).$$

 $B \leftarrow \text{GraefYounesReductionMethod}(\{a^{j_1}, a^{j_2}, \dots, a^{j_p}\})$ 
Output:  $B = \text{ND}(A)$ 

```

Algorithm 2 is an output-sensitive method, i.e., the runtime depends (in addition to the size of the input A) on the size of the output B . More precisely, the worst-case complexity according to [26] can be specified as follows:

$$\mathcal{O}(|A| \log |A| + |A| |B|).$$

If $|B|$ is very small (e.g., $|B| \leq \log |A|$), then Algorithm 2 is very efficient. The calculation of the values $\varphi_\lambda(a^{j_i})$, $i \in \{1, \dots, p\}$, can be efficiently performed by parallelization.

Besides the Graef-Younes method with presorting, also some other non-dominated sorting methods are known in the literature; see, e.g., [36] and [11].

For pattern search type algorithms it is known that the concept of higher level Pareto fronts is useful to achieve a better approximation of the set of efficient solutions [34]. Note that the first level Pareto front is given by $B_1 := \text{ND}(A)$, the second level Pareto front by $B_2 := \text{ND}(A \setminus B_1)$, and generally the level i Pareto front for each $i > 1$ by $B_i := \text{ND}(A \setminus (B_1 \cup \dots \cup B_{i-1}))$. Figure 5 illustrates this concept and shows how a second level and third level front emerge in parallel to the first level front. These higher level fronts can be computed by Algorithm 3.

Algorithm 3 Computing Pareto fronts 1 to k

Input: $A = \{a^1, \dots, a^p\}$, $k \in \mathbb{N}$

Compute an enumeration $\mathcal{A} = \{a^{j_1}, \dots, a^{j_p}\}$ such that

$$\varphi_\lambda(a^{j_1}) \leq \varphi_\lambda(a^{j_2}) \leq \dots \leq \varphi_\lambda(a^{j_p}).$$

for $i = 1$ **to** k **do**
 $B_i \leftarrow \text{GraefYounesReductionMethod}(A \setminus \bigcup_{j=1}^{i-1} B_j)$
end for

Output: B_1, \dots, B_k represent Pareto fronts 1 to k

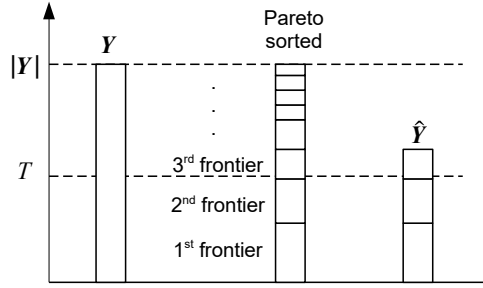


FIGURE 6. Illustration of the ‘Hall of Fame’ updating scheme based on non-dominated sorting and the parameter T .

Algorithm 3 is also an output-sensitive method, with a worst-case complexity of

$$\mathcal{O}\left(|A| \log |A| + |A| \sum_{i=1}^k |B_i|\right).$$

The complexity of calculating all Pareto fronts is therefore given by

$$\mathcal{O}(|A| \log |A| + |A|^2).$$

Note that Algorithm 3 is a novel alternative to the method proposed in [11] for computing all Pareto fronts with quadratic worst-case complexity.

4.4. Formulation of the Multi-Objective Global Pattern Search Algorithm. In this section, we present our Multi-Objective Global Pattern Search Algorithm in full detail. First, as already described in the general scheme of the algorithm in Section 4.3, we use a non-dominated sorting procedure at each iteration of the algorithm (loop ... end loop). In Algorithm 4 (update of the ‘Hall of Fame’) we describe the details of the non-dominated sorting procedure used to generate (first and higher level) Pareto fronts. Starting from a set Y of sampling points, the ‘Hall of Fame’ procedure generates Pareto fronts (starting with level one and then gradually increasing) until at least $\min\{T, |Y|\}$ elements are in the union of the considered Pareto fronts. This union \hat{Y} of Pareto fronts is then used in the Multi-Objective Global Pattern Search Algorithm to define the next set of basis vectors of the pattern search scheme. The update scheme for the ‘Hall of Fame’ is shown schematically in Fig. 6.

Now we are ready to formulate the complete Multi-Objective Global Pattern Search Algorithm (MOGPSA for short) which is given in Algorithm 5. We would like to point out that Algorithm 5 terminates. Indeed, consider an arbitrary iteration k of Algorithm 5 with underlying step widths w_1, \dots, w_n . We claim that there is an iteration $k + l$ (with $l \in \mathbb{N} \cup \{0\}$) so that $\hat{\mathbf{B}} = \mathbf{B}$, hence (if $\max\{w_1, \dots, w_n\} > 1$) the algorithm reaches the last loop line in which the maximum step width of one variable is divided by two. Of course,

Algorithm 4 Update the ‘Hall of Fame’ (function `updateHallOfFame`)Input: The set \mathbf{Y} Compute an enumeration $\mathbf{Y} = \{\mathbf{y}^{j_1}, \dots, \mathbf{y}^{j_{|\mathbf{Y}|}}\}$ such that

$$\varphi_\lambda(\mathbf{y}^{j_1}) \leq \varphi_\lambda(\mathbf{y}^{j_2}) \leq \dots \leq \varphi_\lambda(\mathbf{y}^{j_{|\mathbf{Y}|}}).$$

 $\hat{\mathbf{Y}} \leftarrow \emptyset$ **while** $|\hat{\mathbf{Y}}| < \min\{\mathbb{T}, |\mathbf{Y}|\}$ **do** $\hat{\mathbf{Y}} \leftarrow \hat{\mathbf{Y}} \cup \text{GraefYounesReductionMethod}(\mathbf{Y} \setminus \hat{\mathbf{Y}})$ **end while**Output: The set $\hat{\mathbf{Y}}$ **Algorithm 5** Multi-Objective Global Pattern SearchInput: Problem (MOP) (respectively, (MOP_g)), parameters $\mathbb{T}, \mathbb{N} \in \mathbb{N}$ $\mathbf{w} \leftarrow 2^{\mathbb{N}-1}(1, \dots, 1)$ $\mathbf{B} \leftarrow \{\mathbf{w}\}$ $\mathbf{B}_{\text{all}} \leftarrow \mathbf{B}$ **loop** $S \leftarrow \emptyset$ **for** $\mathbf{b} \in \mathbf{B}$ **do** **for** $i = 1$ **to** n **do** **if** $s_i^+(\mathbf{b}) \in [0, 2^{\mathbb{N}}]^n \setminus \mathbf{B}_{\text{all}}$ **then** $S \leftarrow S \cup \{s_i^+(\mathbf{b})\}$ **end if** **if** $s_i^-(\mathbf{b}) \in [0, 2^{\mathbb{N}}]^n \setminus \mathbf{B}_{\text{all}}$ **then** $S \leftarrow S \cup \{s_i^-(\mathbf{b})\}$ **end if** **end for** **end for** $\mathbf{B}_{\text{all}} \leftarrow \mathbf{B}_{\text{all}} \cup S$ $\mathbf{Y} \leftarrow g[\mathbf{B} \cup S]$ $\hat{\mathbf{Y}} \leftarrow \text{updateHallOfFame}(\mathbf{Y})$ $\hat{\mathbf{B}} \leftarrow g^{-1}[\hat{\mathbf{Y}}] \cap (\mathbf{B} \cup S)$ **if** $\hat{\mathbf{B}} \neq \mathbf{B}$ **then** $\mathbf{B} \leftarrow \hat{\mathbf{B}}$ **continue loop** **end if** **if** $\max\{\mathbf{w}_1, \dots, \mathbf{w}_n\} = 1$ **then** **break loop** **end if** Choose $j \in \{1, \dots, n\}$ such that $\mathbf{w}_j = \max\{\mathbf{w}_1, \dots, \mathbf{w}_n\}$ $\mathbf{w}_j \leftarrow \mathbf{w}_j/2$ **end loop** $\hat{\mathbf{Y}} \leftarrow \text{GraefYounesReductionMethod}(\hat{\mathbf{Y}})$ $\hat{\mathbf{B}} \leftarrow g^{-1}[\hat{\mathbf{Y}}] \cap \mathbf{B}$ Output: The sets $h[\hat{\mathbf{B}}] \subseteq [\mathbf{x}^-, \mathbf{x}^+]$ and $\hat{\mathbf{Y}} \subseteq f[[\mathbf{x}^-, \mathbf{x}^+]]$

the condition $\hat{\mathbf{B}} = \mathbf{B}$ can occur in an iteration $k + l$ with $S \neq \emptyset$. Otherwise, $\hat{\mathbf{B}} = \mathbf{B}$ occurs in an iteration $k + l$ with $S = \emptyset$, taking into account that there are only finitely many integer grid points in $[0, 2^{\mathbb{N}}]^n$. Consequently, the step widths $\mathbf{w}_1, \dots, \mathbf{w}_n$ fulfill the

condition $\max\{\mathbf{w}_1, \dots, \mathbf{w}_n\} = 1$ after a finite number of iterations. The break command then ends the loop.

4.5. Comments related to the algorithm. First of all, we would like to reflect about the choice of the algorithm parameter T .

Clearly, for $T \geq 1$ the set \hat{Y} generated by the 'Hall of Fame' procedure (as part of Algorithm 5) always contains the first level Pareto front $ND(Y)$.

If $T = 1$, then $\min\{T, |Y|\} = 1$, so the 'Hall of Fame' procedure generates nothing else than the first level Pareto front $ND(Y)$.

If $T \geq |G_{\mathbb{Z}}|$ one has $\hat{B} = B \cup S$ after the 'Hall of Fame' procedure. Then, at the end of the algorithm (after the loop), a non-dominated (first level) sorting is applied to all points in $g[G_{\mathbb{Z}}]$, i.e., $\hat{Y} = ND(g[G_{\mathbb{Z}}])$. If N has a sufficiently large value, one obtains a good approximation of the box $h[[0, 2^N]^n] = [x^-, x^+]$ and thus a good approximation of the set of efficient solutions $Eff([x^-, x^+] | f)$.

Based on the above observations (and some numerical experience), one can expect that our algorithm achieves a better global behavior with respect to the approximation of the set of efficient solutions $Eff([x^-, x^+] | f)$ if one increases T (and chooses a sufficiently large value for N). Of course, the drawback is that an increased parameter T often leads to a higher numerical effort for computing the sets \hat{B} and \hat{Y} . In particular, this is the case if the calculation of the objective function values of the given sampling points is very costly, as in our bi-objective damage location problem in Section 3.3. It is clear that a parallel evaluation of the function values of the given sampling points is useful, especially for a larger T with a higher number of sampling points.

In practice, when choosing T (and N) for a specific problem, the decision-maker has to gain experience with the Algorithm 5 with regard to the expected approximation quality and the time supply.

Considering that calculating the objective function values of sampling points can be very costly in practice, it is important in an effective implementation of Algorithm 5 to store the assignment between sampling points and corresponding calculated image points (using a cache structure). This means that one should avoid to recalculate $g(\mathbf{b})$ for $\mathbf{b} \in B \cup S$ (statement $Y \leftarrow g[B \cup S]$ in Algorithm 5), if \mathbf{b} is already known from previous iterations. Using the assignment between sampling points and corresponding image points, the statements $\hat{B} \leftarrow g^{-1}[\hat{Y}] \cap (B \cup S)$ and $\hat{B} \leftarrow g^{-1}[\hat{Y}] \cap \hat{B}$, which are given in Algorithm 5, can be effectively implemented as well.

In the following part of the section, we relate our approach to other approaches known from the literature.

First of all, if we apply MOGPSA to the single-objective case (i.e., $m = 1$ in the problem (MOP)), we basically obtain the (Single-Objective) Global Pattern Search Algorithm (GPSA) proposed in [27]. In this case, for each set $A \subseteq \mathbb{R} \cup \{+\infty\}$, we have

$$ND(A) = \{a \in A \mid a \notin A \setminus \{a\} + \mathbb{R}_+^m\} = \{a \in A \mid \nexists \bar{a} \in A: \bar{a} < a\}.$$

The non-dominated sorting procedure according to the Algorithm 2 is therefore basically a sorting of finitely many numbers in $\mathbb{R} \cup \{+\infty\}$ and the selection of the smallest element.

MOGPSA belongs to the class of deterministic derivative-free pattern search methods for approximating solutions to multi-objective optimization problems, especially problems with expensive objective functions. Clearly, it shares the pattern search feature with other algorithms known in (single and multi-objective) optimization; see, e.g., [28, 50, 12, 1, 10, 9, 27] and the references therein. According to [9] our algorithm belongs to the class of direct search methods. Some well-known deterministic derivative-free methods for multi-objective optimization problems are proposed in [10, 9, 18], while non-deterministic (hybrid) methods are proposed in [11, 32, 10], and many other publications related to evolutionary (population-based) multi-objective optimization; see [9] for a survey on this topic. Non-dominated sorting for computing first and higher level Pareto fronts based on a new

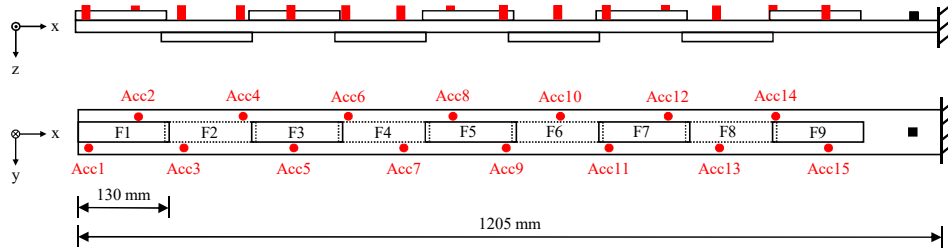


FIGURE 7. Schematic overview of the steel cantilever beam with nine screwed-on fishplates F1 to F9, 15 sensor positions (red points), and the position of excitation (black square).

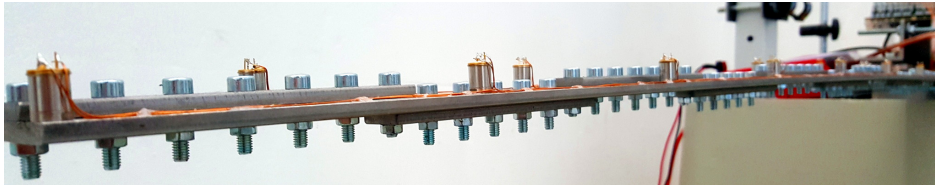


FIGURE 8. Photograph of the steel cantilever beam.

procedure with quadratic worst-case complexity (see Algorithm 3) is a key feature of our algorithm, similar to NSGA-II in [11] but in contrast to the Direct Multisearch Method in [10] and MOSAST in [32, 38] where only the first level Pareto front is used. MOG-PSA has only two input parameters T and N which have an influence on the quality of the approximation of solutions of the multi-objective optimization problem (MOP). Numerical experience with our Algorithm 5 shows that the set \hat{Y} generated by the 'Hall of Fame' procedure is often larger at late iterations, since then many first-level (and possibly higher level) non-dominated points are contained in \hat{Y} (notice again that we always have $ND(Y) \subseteq \hat{Y}$ in the 'Hall of Fame' procedure), which is a useful feature of our algorithm to obtain (in the best case) a good approximation of the Pareto front of the problem (MOP). However, as noted above, the choice of T is also important in order to have sufficiently many points in \hat{Y} generated by the 'Hall of Fame' procedure in early iterations. In particular, this means that the number of (first or higher level) non-dominated points considered at each iteration of our Algorithm 5 generally does not remain constant. This is in contrast to certain evolutionary algorithms, such as NSGA-II in [11], where only a constant number of non-dominated points are used at each iteration of such algorithms (possibly not including complete Pareto fronts). For instance, such a reduction in the number of (first or higher level) non-dominated points is achieved in NSGA-II by using a crowding distance metric.

5. COMPUTATIONAL RESULTS

We test the proposed optimization algorithm and demonstrate its applicability on two example problems: a cantilever beam and a girder mast. In both cases we introduce a controllable artificial damage by local modifications of the structural properties. As our focus is on the practical application here, we do not evaluate the algorithmic performance.

5.1. Laboratory beam experiment. As a first numerical example, a laboratory cantilever beam structure is chosen. Measurement data obtained from an experimental steel beam with reversible damage mechanisms presented in Wolniak et al. [52] is utilized. Figures 7 and 8 show a schematic overview as well as a photograph of the cantilever beam; the artificial damage mechanism is shown in Fig. 9.

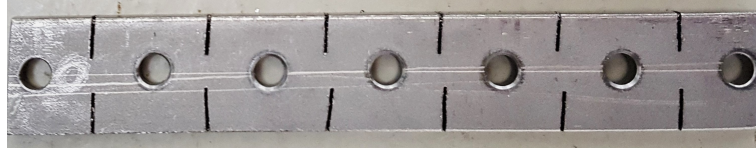


FIGURE 9. Photograph of reversible damage mechanism for cantilever beam, i.e., damaged fishplate.

5.1.1. *Experimental Setup.* Nine fishplates are mounted to the top and bottom of a central beam. They can be replaced with damaged fishplates to reduce the stiffness at various positions (F1 to F9 in Fig. 7). The fishplates are damaged by uniformly distributed sawcuts on both sides of the plate, as illustrated in Fig. 9. Thus, replacing an undamaged fishplate with a damaged one reduces the stiffness at known positions. The damage leads to a decrease in the eigenfrequencies of the structure as well as to alterations in the bending mode shapes. In order to identify the modal parameters, a contact-free electromagnetic shaker is positioned close to the root of the beam (black square in Fig. 7) and used to excite the structure with a broadband white noise excitation signal with up to 250 Hz. Fifteen IEPE acceleration sensors of the type MEAS 805-0005-01 are placed uniformly along the length of the beam and record the resulting vibration (Acc1 to Acc15 in Fig. 7). The electrical signals provided by the sensors are recorded with an HBK QuantumX MX1601B data acquisition system using analog-to-digital conversion with 24-bit resolution and a sampling rate of 1200 Hz. A detailed description of the experiment is given in Wolniak et al. [52]. The modal parameters Φ_k and f_k are identified from time-domain measurements with a duration of one minute each as described in Section 3.3. For model updating, the identification results obtained for the reference state represent the measured healthy state M0, as defined in Table 1. The identification results of the nine damage scenarios are considered as the analysis state M1.

The beam is uniformly discretized into 241 elements of length 5 mm which obey Bernoulli linear beam theory (Section 3.1). As the cantilever beam has sections of varying thickness, as well as additional sensor and screw masses, the cross-sectional area A_e , the linear density $\ell_e \rho_e$ and the area moment of inertia I_e of the beam elements must be calculated accordingly. The fishplates are mounted on either side of the beam in an alternating pattern with a small overlap between them along the length of the beam, resulting in beam elements with a combined cross-sectional area of the beam and one fishplate along with elements with a combined cross-sectional area of the beam and two fishplates. The varying cross sections are taken into account when calculating the beam element's area moment of inertia. This is done by adding either one or two times the fishplate's moment of inertia on top of the beam's. Finally the linear density is calculated, accounting for varying cross sections. In addition, the sensor masses are considered by adding them in the form of an equivalent linear density at the appropriate positions. Screw masses are accounted for by a uniformly distributed linear density on every element.

The finite element model is created and assembled in Matlab using the varying properties of the beam elements. Mechanical parameters of this structure are given in Table 2. Damage is modeled by reducing the element stiffness according to the Gaussian damage distribution with parameters $\mathbf{x} = (D, \mu, \sigma)$ presented in Section 3.2.

We consider nine damage scenarios obtained by replacing exactly one of the fishplates F_i with a damaged one. The Gaussian distribution model intentionally differs from the uniform distribution used to damage the fishplates. The damage distribution is parameterized according to the formulation introduced in Section 3.1 using the center of damage μ , the damage severity D and the damage extent σ . For each of the nine damage scenarios we know the center μ but we cannot compute the exact values of σ and D . The domain

TABLE 2. Properties of the steel cantilever beam.

Property	Value
Elastic Modulus	127 GPa
Beam Length	1205 mm
Beam Height	5.15 mm
Beam Width	60 mm
Fishplate Height	4.85 mm
Fishplate Width	2 mm
Density	7800 kg/m ³

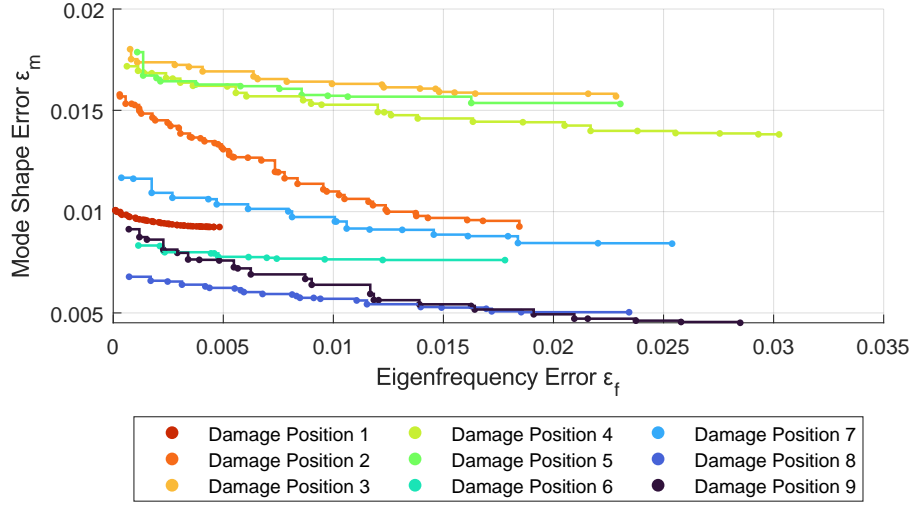


FIGURE 10. Non-dominated points belonging to the stiffness scaling factor distributions shown in Fig. 11.

of optimization is given by the bounds described in Section 3.2, with $D_{\max} = 0.3$ for the severity $D \in [0, D_{\max}]$ and with length $L = 1205$ mm for $\mu, \sigma \in [0, L]$. The constraint for the stiffness scaling factors is enforced below $\theta_{\min} = 0.15$. These values are chosen such that the considered damage scenarios are situated inside the domain.

5.1.2. Computational Results. Our Algorithm 5 (MOGPSA) is run with its parameters set to $T = 50$ and $N = 20$, and with 1000 objective function evaluations for each of the damage scenarios. The resulting (first level) Pareto fronts in the objective space are shown in Fig. 10. We observe that all nine Pareto fronts are asymmetric with respect to the first bisector. In particular, the fronts show small variations of the mode shape error and large variations of the eigenfrequency error. The number of computed non-dominated points varies between the different damage scenarios as it depends on the specific instance of the optimization problem. Note that the computed points on each front are not interpolated by a polygonal path (as usual) but rather by concave pairs of horizontal and vertical line segments. This guarantees that the computed fronts, including the connections, are feasible: they belong to the extended image set $f[\Omega] + \mathbb{R}_+^2$, which is bounded by the unknown true Pareto front to the lower left.

The numbers of computed points for all nine Pareto fronts are listed in Table 3 with minimal, average and maximal values of each damage parameter and in Table 4 with the corresponding values of each error measure. Positions and values of μ and σ refer to beam elements and need to be multiplied by 5 mm to obtain length values.

TABLE 3. Cantilever beam: distribution statistics of Pareto-optimal damage parameters for all nine scenarios. DP = actual damage position (beam element), # = size of Pareto-optimal data set.

DP	#	μ			σ			D		
		min	avg	max	min	avg	max	min	avg	max
15	49	1.00	8.40	17.25	3.39	8.70	14.31	0.0224	0.0432	0.0563
39	47	24.75	32.76	37.25	4.27	8.67	15.19	0.0229	0.0332	0.0510
63	19	56.00	58.77	61.00	3.39	5.25	8.16	0.0208	0.0305	0.0432
87	27	82.25	85.08	87.25	2.39	5.32	8.54	0.0167	0.0281	0.0479
111	12	104.75	107.25	109.75	2.13	4.52	9.29	0.0151	0.0253	0.0391
135	13	129.75	132.25	136.00	2.51	5.36	9.16	0.0167	0.0280	0.0474
159	20	156.00	157.63	159.75	2.01	4.92	7.53	0.0146	0.0279	0.0438
183	23	174.75	176.27	178.50	4.90	6.99	9.29	0.0229	0.0327	0.0417
207	25	199.75	201.40	203.50	2.76	5.54	8.91	0.0182	0.0292	0.0495

TABLE 4. Cantilever beam: distribution statistics of error measures for all nine scenarios. DP = actual damage position (beam element). # = size of Pareto-optimal data set.

DP	#	ϵ_f			ϵ_m		
		min	avg	max	min	avg	max
15	49	0.000096	0.0024	0.0048	0.0092	0.0095	0.01007
39	47	0.000294	0.0066	0.0185	0.0093	0.0126	0.01578
63	19	0.000767	0.0099	0.0228	0.0157	0.0165	0.01802
87	27	0.000621	0.0120	0.0303	0.0138	0.0153	0.01717
111	12	0.001089	0.0077	0.0230	0.0153	0.0162	0.01787
135	13	0.001142	0.0063	0.0178	0.0076	0.0079	0.00833
159	20	0.000370	0.0103	0.0254	0.0084	0.0097	0.01167
183	23	0.000720	0.0092	0.0234	0.0050	0.0058	0.00678
207	25	0.000707	0.0111	0.0285	0.0045	0.0064	0.00913

Figure 11 shows the stiffness distribution functions, each corresponding to a point on the respective Pareto front, for all nine damage scenarios. The correct damage positions for all damage scenarios are indicated with dashed lines. The Pareto-optimal damage distributions show that all damage positions are estimated in the correct order. Furthermore, all damage positions are located closely to the actual damage position and possess a similar severity of the estimated damage. The damage severity D, which corresponds to the area enclosed by the distributions, has similar values for most of the optimal distributions. This is consistent with the expected result, as all damage scenarios are implemented with the same damaged fishplate and hence the damage severity should be approximately equal regardless of the position. Additionally, the widths of the depicted damage distribution functions are consistent with each other, which also matches the actual experiment. Minor deficiencies in the accuracy of the beam modeling due to material irregularities and faulty model properties can cause slight deviations in the damage position, which can be seen throughout most given results.

Overall, these findings confirm that the model updating method as well as the optimization algorithm fulfill their respective tasks. The location is adequately accurate for all scenarios considered. All values of D and σ are well below their upper bounds and thus well within the search area. Additionally, the results confirm that an a-priori weighting between

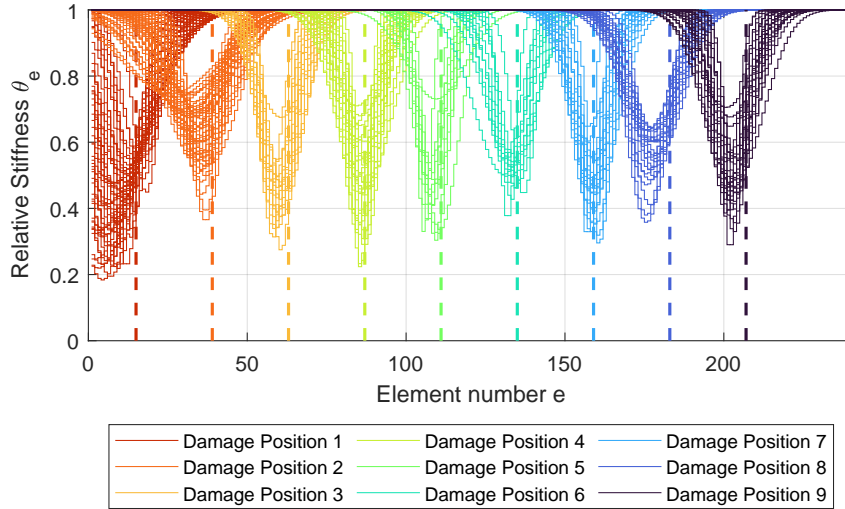


FIGURE 11. Plot of the stiffness scaling factor distributions identified for multiple different damage positions on the experimental beam. Scaling factors are plotted using continuous lines, true damage positions are plotted using dashed lines.

eigenfrequency errors and mode shape errors does not make sense in practice: most of the Pareto fronts cover wide ranges of the error measures, in particular of the eigenfrequency error, and therefore a single point on each front would give insufficient information. Taking a look at Figure 10, it appears that each Pareto front is part of the boundary of a *convex* extended image set $f[\Omega] + \mathbb{R}_+^2$, and therefore every front also seems to be computable by weighted sum (linear) scalarization, i.e., by solving a series of scalarized optimization problems which involve convex combinations of the objective functions ε_f and ε_m . Note that for each of these problems, the scalar objective function is also expensive as the sum of the expensive functions ε_f and ε_m . In order to obtain a good approximation of the Pareto fronts, the weighted sum scalarization approach would therefore require to solve a whole series of expensive problems, e.g., with classical pattern search algorithms.

5.2. Girder mast structure. As a more complex and particularly difficult numerical example we consider a girder mast structure. The mast is made of construction steel and situated in an outdoor test facility illustrated in Fig. 12. The structure is dynamically excited by environmental conditions such as wind forces and micro-seismic vibrations from the ground. The whole setup is introduced in detail by Wernitz et al. [51].

5.2.1. Experimental setup. The mast is 9 m tall with triangular cross-section. It consists of three vertical segments, each made up of seven sub-segments called bays. Each bay has three vertical cylindrical pipes that are connected at the top and at the bottom by horizontal triangles made of massive cylindrical cross struts with smaller diameter, and by three inclined cross struts of the same type in between, see Fig. 13. Each segment has three additional vertical pipes at each end, where the segments are connected to each other without further cross struts. The finite element model is assembled semi-automatically in the commercial simulation software Abaqus. Herein the order of beams is determined internally in a reasonable way that keeps neighboring beams closely together. For the girder mast there is of course no natural linear order of the beams. All pipes (legs) and struts (braces) are modeled as Timoshenko beams according to Section 3.1; they are uniformly discretized with three elements per horizontal beam, four elements per vertical beam and five elements per inclined beam. Five of the six additional vertical beams that connect segments consist of

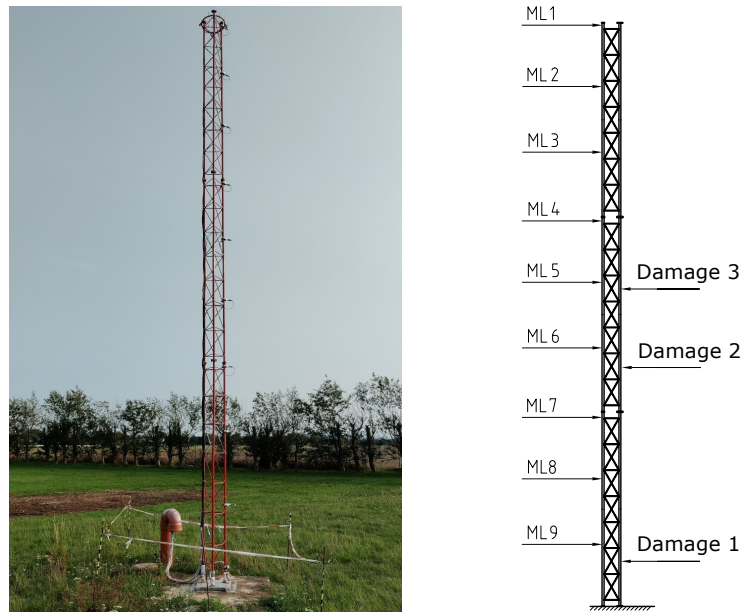


FIGURE 12. Girder mast structure: Photograph (left) and sketch with damage position (right).



FIGURE 13. Photograph of reversible damage mechanisms integrated into the struts of the girder mast structure.

one element each, the sixth beam consists of two elements to account for a sensor. Altogether we have 198 beams with a total of 804 finite elements. Finally there is a horizontal circular steel ring mounted at the mast top (see Fig. 12 left) which is modeled as a point mass. Materials and cross-sections are assigned according to the as-measured dimensions of the structure, which are summarized in Table 5. In this table, the nonstructural mass due to welding material, paint and zinc coating is included in the density, while point masses for the tower head, sensors and cables are specified separately.

Structural acceleration is measured using 18 piezoelectric accelerometers of type MEAS 8811LF-01, situated on the nine measurement levels indicated by ML1 to ML9 in Fig. 12. Sensor signals are continuously converted to digital data using National Instruments NI-9234 cards at a sampling frequency of 1651.61 Hz, and the data is streamed to an off-site

TABLE 5. Properties of the girder mast structure

Property	Value
Elastic Modulus	210 GPa
Outer diameter legs	30 mm
Wall thickness legs	3 mm
Diameter braces	10 mm
Bay height	0.4 m
Density including nonstructural mass	8670 kg/m ³
Sensor node mass	0.45 kg
Head mass	2.97 kg
Cable mass	3.19 kg

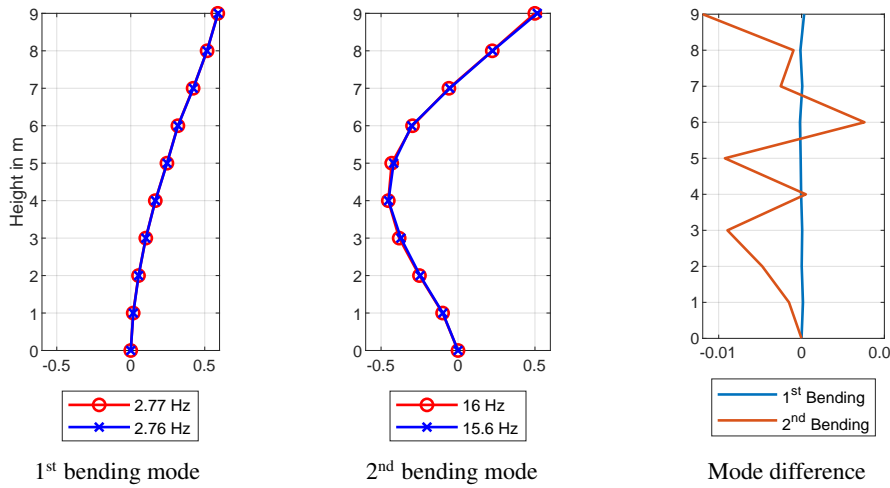


FIGURE 14. Mode shapes and eigenfrequencies identified from measurement data for the structure shown in Fig. 12, as well as the difference between the healthy state and damage at position 1. Undamaged state indicated by red lines, damage at position 1 indicated by blue lines.

data storage server. In addition to the continuous measurement of the vibration, material temperature and meteorological data is also captured and available for further processing.

Structural damage is introduced by cutting braces at three distinct positions of the structure, as indicated in Fig. 12. The damage mechanism is depicted in Fig. 13 and shows the removable struts which replace the otherwise solid diagonal bracings. In the damaged scenarios, a single diagonal brace is removed at the respective position along the structure. The modal parameters Φ_k and f_k of the structure are identified from 10-minute data sets as described in Section 3.3. One of the data sets was recorded before the damage event and the other one thereafter. The data sets are chosen so that the vibration amplitudes as well as the material temperature are roughly the same. This way, data contamination due to differing environmental conditions is prevented. The identified modes shapes and eigenfrequencies of the structure are shown in Fig. 14 for the undamaged state and the data set recorded for damage position 1, respectively. Additionally, the differences in the mode shapes with respect to the damage are shown in a separate panel in the same figure.

The modal analysis of the model is carried out using the finite element solver Abaqus. The simulated mode shapes for the undamaged structure, as shown in in Fig. 15, resemble the identified mode shapes.

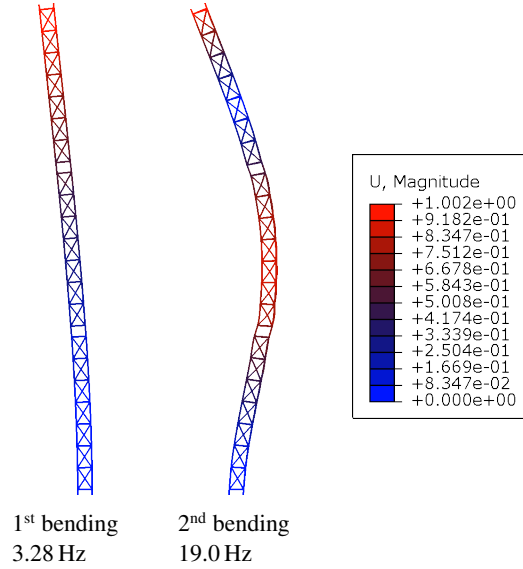


FIGURE 15. Finite element simulation results for mode shapes and eigenfrequencies of the undamaged state.

The mode shapes taken into account in the model updating procedure belong to the first two bending mode pairs of the structure. The eigenfrequencies drop consistently, as expected when reducing the stiffness of the structure. Our single-beam damage model is not entirely adequate for the girder mast structure because the beams are connected in a complex 3D pattern rather than a linear sequence; hence we need to make slight adaptations. We assume that only a single beam is damaged and confine the optimization to the box $(D, \mu, \sigma) \in [0, 0.02] \times [0, 804] \times [0, 10]$. Thus, the total length of the structure (the number of beam elements) is our upper bound for the damage center μ whereas a fictitious longest single beam consisting of ten elements determines the upper bound for the extent σ . This includes a safety margin over the true maximal length of five elements. The lower bound on the stiffness scaling factors is enforced with parameter $\theta_{\min} = 0.01$.

5.2.2. Computational results. Our Algorithm 5 (MOGPSA) is run with 5000 objective function evaluations using $T = 30$ and $N = 20$. The resulting (first level) Pareto fronts are shown in Fig. 16. The computed points on the front are again connected by concave pairs of horizontal and vertical line segments to visualize the space dominated by these solutions. Overall, a large number of non-dominated points were found, which suggests that the parameters T and N of the MOGPS algorithm are adequately chosen. The Pareto fronts have a greatly varying density of solutions and they exhibit large gaps and concave features. Hence, in this problem, the corresponding parts of the fronts cannot be computed by the weighted sum (linear) scalarization technique whereas the non-dominated sorting approach implemented in our algorithm provides all the information required in practical applications.

The minimal, median and maximal values of each damage parameter and each error measure, respectively, are listed in Tables 6 and 7. Positions and values of μ and σ refer again to beam elements. As mentioned, the order of beams is determined by the Abaqus software, and here it is arbitrary since the beams of the mast do not form a linear sequence. We choose the medians of the distributions here rather than the average since the computed Pareto optimal points form two clusters (in contrast to a single cluster for the steel beam). These clusters turn out to correspond to respective subsets of points associated with correct and incorrect damage locations, see next paragraph.

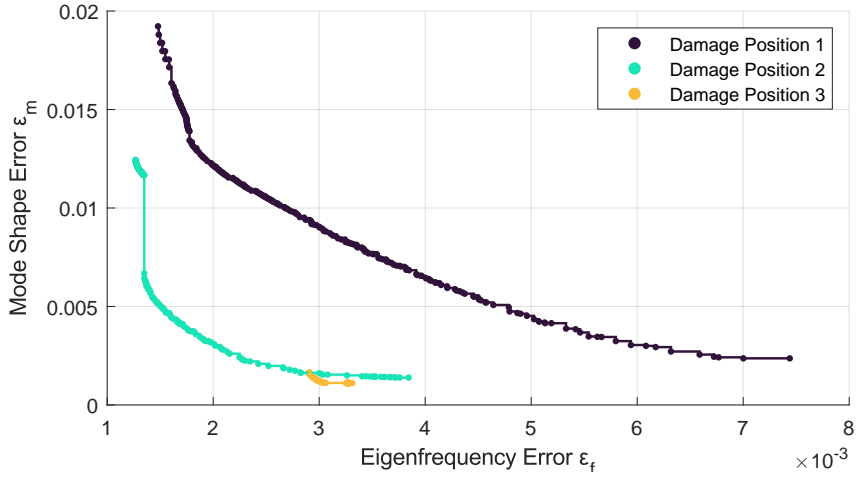


FIGURE 16. Pareto frontier of the girder mast model updating problem.

TABLE 6. Girder mast: distribution statistics of Pareto-optimal damage parameters for all three scenarios. DP = actual damage position (beam element), # = size of Pareto-optimal data set.

DP	#	μ			σ			$D \times 1000$		
		min	median	max	min	median	max	min	median	max
6	262	3.48	9.63	163.06	4.68	6.34	7.88	14.6	15.9	18.3
274	179	273.12	276.51	358.72	1.95	2.27	4.73	6.1	6.8	13.7
429	667	1.01	437.27	804	1e-4	0.11	10	0	0.24	4.5

TABLE 7. Girder mast: distribution statistics of error measures for all three scenarios. DP = actual damage position (beam element), # = size of Pareto-optimal data set.

DP	#	ε_f			ε_m		
		min	median	max	min	median	max
6	262	0.0015	0.0026	0.0074	0.0024	0.0103	0.0192
274	179	0.0013	0.0014	0.0038	0.0014	0.0057	0.0124
429	667	0.0029	0.0029	0.0033	0.0011	0.0016	0.0016

The non-dominated stiffness distributions for all three damage positions are shown in Fig. 17. Dashed lines in the corresponding colors indicate the exact damage positions. Each colored curve shows an overlay of several curves corresponding to the individual non-dominated points. A major part of the optimal damage distributions show the estimated damage position close to the actual damage position: 121 for damage position one, 83 for damage position two, and 573 for damage position three. However, we also observe 141, 96 respectively 94 optimal damage distributions that identify the wrong beam as damaged.

The obtained results show that the presented model updating procedure enables a precise damage location for all investigated damage positions. A fraction of solutions for all damage positions seem to identify the damage position far from the actual position. This is due to the bracings in the finite elements not being sorted in any particular order when applying the damage distribution. In fact, the addressed damage distributions all identify

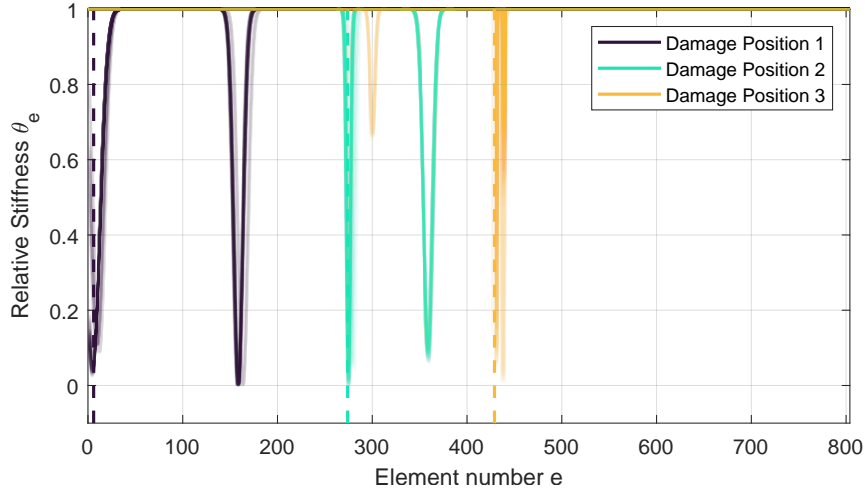


FIGURE 17. Stiffness scaling factors computed for the Pareto fronts. MOGPS results are shown using solid lines and position of experimentally damaged bay is indicated using dashed lines.

the maximum damage on diagonal braces close to the correct position, since neighboring damage positions tend to have a similar impact on the dynamic behavior of the structure. Finally, most of the Pareto-optimal solutions possess a minimum relative stiffness close to zero, which is consistent with the experiment, where the diagonal braces are completely removed. This further strengthens the results as all of the computed damage distributions have minimum relative stiffnesses near zero.

6. CONCLUSION

The application of the multi-objective model updating scheme to the two experimental structures yields satisfactory results overall. The proposed pattern-search algorithm is capable of finding non-dominated solutions effectively and structural damage is located adequately. The results for the laboratory beam experiment are almost perfect. The damage location in the girder mast example is ambiguous since a fraction of the non-dominated solutions point to damage positions next to the actual damage. This is not surprising as the one-dimensional damage model cannot adequately capture the complex three-dimensional connection topology of the individual beams. In spite of this, our approach does detect the presence of a damage reliably and narrows down the damage center to just two possible locations, which is still good enough from a practical point of view.

Regarding the proposed optimization algorithm, there is room for future research. A subsequent theoretical analysis should address questions about the approximation quality of computed Pareto optimal points and the quality of coverage of the Pareto front. Further, numerical benchmarks using academic test problems and additional application problems should be conducted to evaluate the performance of the algorithm, to study the influence of the parameters T and N , and to compare it to other algorithms from the literature.

ACKNOWLEDGEMENT

The third author wishes to thank for the financial support by the Deutsche Forschungsgemeinschaft (DFG, German Research Foundation) – SFB1463 – 434502799, subproject C04. The fifth author is funded by the Federal Ministry for Economic Affairs and Energy *MMRB-Repair-care – Multivariate damage monitoring of rotor blades: implementation and analysis of the effects of repair measures*, FKZ 03EE2043C. The sixth and seventh

authors gratefully acknowledge the financial support by the Deutsche Forschungsgemeinschaft – SFB 1463 – 434502799, subproject B05.

REFERENCES

- [1] M. A. ABRAMSON, *Second-order behavior of pattern search*, SIAM Journal on Optimization, 16 (2005), pp. 515–530.
- [2] P. ALOTTO AND G. CAPASSO, *A deterministic multiobjective optimizer*, COMPEL: The International Journal for Computation and Mathematics in Electrical and Electronic Engineering, 34 (2015), pp. 1351–1363.
- [3] R. ANDREANI, A. L. CUSTÓDIO, AND M. RAYDAN, *Using first-order information in direct multisearch for multiobjective optimization*, Optim. Methods Softw., 37 (2022), pp. 2135–2156.
- [4] S.-K. AU, *Fast Bayesian ambient modal identification in the frequency domain, part II: Posterior uncertainty*, Mechanical Systems and Signal Processing, 26 (2012), pp. 76–90.
- [5] O. BEGAMBRE AND J. LAIER, *A hybrid Particle Swarm Optimization – Simplex algorithm (PSOS) for structural damage identification*, Advances in Engineering Software, 40 (2009), pp. 883–891.
- [6] M. BRUNS, B. HOFMEISTER, C. HÜBLER, AND R. ROLFES, *Damage localization via model updating using a damage distribution function*, in Structural Health Monitoring 2019, Lancaster, PA, 2019, DEStech Publications, Inc, pp. 1–10.
- [7] C. A. COELLO COELLO, *Theoretical and numerical constraint-handling techniques used with evolutionary algorithms: A survey of the state of the art*, Computer Methods in Applied Mechanics and Engineering, 191 (2002), pp. 1245 – 1287.
- [8] C. A. COELLO COELLO, G. T. PULIDO, AND M. S. LECHUGA, *Handling multiple objectives with particle swarm optimization*, IEEE Transactions on Evolutionary Computation, 8 (2004), pp. 256–279.
- [9] A. CUSTÓDIO, M. EMMERICH, AND J. MADEIRA, *Recent developments in derivative-free multiobjective optimization*, Computational Technology Reviews, 5 (2012), pp. 1–31.
- [10] A. L. CUSTÓDIO, J. A. MADEIRA, A. I. F. VAZ, AND L. N. VICENTE, *Direct multisearch for multiobjective optimization*, SIAM Journal on Optimization, 21 (2011), pp. 1109–1140.
- [11] K. DEB, S. AGRAWAL, A. PRATAP, AND T. MEYARIVAN, *A fast elitist non-dominated sorting genetic algorithm for multi-objective optimization: NSGA-II*, in Parallel Problem Solving from Nature PPSN VI, Berlin, Heidelberg, 2000, Springer Berlin Heidelberg, pp. 849–858.
- [12] E. DOLAN, R. LEWIS, AND V. TORCZON, *On the local convergence of pattern search*, SIAM Journal on Optimization, 14 (2003), pp. 567–583.
- [13] F. Y. EDGEWORTH, *Mathematical Psychics*, McMaster University Archive for the History of Economic Thought, 1881.
- [14] M. EHRGOTT, *Multicriteria Optimization*, Springer-Verlag, Berlin, second ed., 2005.
- [15] G. EICHFELDER, *Twenty years of continuous multiobjective optimization in the twenty-first century*, EURO Journal on Computational Optimization, 9 (2021).
- [16] G. EICHFELDER, P. KIRST, L. MENG, AND O. STEIN, *A general branch-and-bound framework for continuous global multiobjective optimization*, J. Global Optim., 80 (2021), pp. 195–227.
- [17] G. EICHFELDER, K. KLAMROTH, AND J. NIEBLING, *Nonconvex constrained optimization by a filtering branch and bound*, J. Global Optim., 80 (2021), pp. 31–61.
- [18] Y. EVTUSHENKO AND M. POSYPKIN, *A deterministic algorithm for global multi-objective optimization*, Optimization Methods and Software, 29 (2014), pp. 1005–1019.
- [19] W. FAN AND P. QIAO, *Vibration-based damage identification methods: A review and comparative study*, Structural Health Monitoring, 10 (2011), pp. 83–111.
- [20] J. FLIEGE, L. M. GRAÑA DRUMMOND, AND B. F. SVAITER, *Newton’s method for multiobjective optimization*, SIAM J. Optim., 20 (2009), pp. 602–626.
- [21] J. FLIEGE AND B. F. SVAITER, *Steepest descent methods for multicriteria optimization*, Math. Methods Oper. Res., 51 (2000), pp. 479–494.
- [22] M. I. FRISWELL, *Dynamics of Rotating Machines*, Cambridge university press, 2010.
- [23] M. I. FRISWELL AND J. E. MOTTERSHEAD, *Finite Element Model Updating in Structural Dynamics*, vol. 38 of Solid Mechanics and its Applications, Springer Netherlands, 1995.
- [24] L. M. GRAÑA DRUMMOND AND B. F. SVAITER, *A steepest descent method for vector optimization*, J. Comput. Appl. Math., 175 (2005).
- [25] C. GÜNTHER, E. KÖBIS, P. SCHMÖLLING, AND C. TAMMER, *Vectorial penalisation in vector optimisation in real linear-topological spaces*, Journal of Nonlinear and Variational Analysis, 7 (2023), pp. 651–686.
- [26] C. GÜNTHER AND N. POPOVICI, *New algorithms for discrete vector optimization based on the Graef-Younes method and cone-monotone sorting functions*, Optimization, 67 (2018), pp. 975–1003.
- [27] B. HOFMEISTER, M. BRUNS, AND R. ROLFES, *Finite element model updating using deterministic optimization: A global pattern search approach*, Engineering Structures, 195 (2019), pp. 373 – 381.
- [28] R. HOOKE AND T. A. JEEVES, *“Direct search” solution of numerical and statistical problems*, J. ACM, 8 (1961), pp. 212–229.

- [29] D. L. HUNT, *Application of an enhanced coordinate modal assurance criterion*, in 10th International modal analysis conference, vol. 1, 1992, pp. 66–71.
- [30] M. M. JAHJOUH, *A Modified Adaptive Harmony Search Algorithm Approach on Structural Identification and Damage Detection*, Institut für Baumechanik und Numerische Mechanik, Gottfried Wilhelm Leibniz Universität Hannover, Hannover, 2016.
- [31] M. M. JAHJOUH AND U. NACKENHORST, *1876. A modified harmony search approach on structural identification and damage detection of wind turbine supporting structures.*, Journal of Vibroengineering, 18 (2016).
- [32] J. JAHN, *Multiobjective search algorithm with subdivision technique*, Computational Optimization and Applications, 35 (2006), pp. 161–175.
- [33] J. JAHN, *Vector Optimization*, Springer-Verlag, Berlin, second ed., 2011. Theory, applications, and extensions.
- [34] D. KALYANMOY ET AL., *Multi Objective Optimization Using Evolutionary Algorithms*, John Wiley and Sons, 2001.
- [35] G.-H. KIM AND Y.-S. PARK, *An improved updating parameter selection method and finite element model update using multiobjective optimisation technique*, Mechanical Systems and Signal Processing, 18 (2004), pp. 59–78.
- [36] H. T. KUNG, F. LUCCIO, AND F. P. PREPARATA, *On finding the maxima of a set of vectors*, J. ACM, 22 (1975), pp. 469–476.
- [37] R. LEVIN AND N. LIEVEN, *Dynamic finite element model updating using simulated annealing and genetic algorithms*, Mechanical Systems and Signal Processing, 12 (1998), pp. 91–120.
- [38] S. LIMMER, D. FEY, AND J. JAHN, *GPU implementation of a multiobjective search algorithm*, Positivity, 16 (2012), pp. 397 – 404.
- [39] M. LINK, *Updating of analytical models—review of numerical procedures and application aspects*, in Proc., Structural Dynamics Forum SD2000, Research Studies Press, Baldock, UK, 1999, pp. 193–223.
- [40] J. E. MOTTERSHEAD AND M. I. FRISWELL, *Model updating in structural dynamics: A survey*, Journal of Sound and Vibration, 167 (1993), pp. 347–375.
- [41] J. NARANJO-PÉREZ, M. INFANTES, J. FERNANDO JIMÉNEZ-ALONSO, AND A. SÁEZ, *A collaborative machine learning-optimization algorithm to improve the finite element model updating of civil engineering structures*, Engineering Structures, 225 (2020), p. 111327.
- [42] J. NIEBLING AND G. EICHFELDER, *A branch-and-bound-based algorithm for nonconvex multiobjective optimization*, SIAM J. Optim., 29 (2019), pp. 794–821.
- [43] V. PARETO, *Cours D’Economie Politique*, F. Rouge, 1896.
- [44] Ø. W. PETERSEN AND O. ØISETH, *Sensitivity-based finite element model updating of a pontoon bridge*, Engineering Structures, 150 (2017), pp. 573–584.
- [45] K. SCHRÖDER, C. G. GEBHARDT, AND R. ROLFES, *A two-step approach to damage localization at supporting structures of offshore wind turbines*, Structural Health Monitoring, 17 (2018), pp. 1313–1330.
- [46] E. SIMOEN, G. DE ROECK, AND G. LOMBAERT, *Dealing with uncertainty in model updating for damage assessment: A review*, Mechanical Systems and Signal Processing, 56-57 (2015), pp. 123–149.
- [47] A. TEUGHELIS, G. DE ROECK, AND J. A. SUYKENS, *Global optimization by coupled local minimizers and its application to FE model updating*, Computers & Structures, 81 (2003), pp. 2337–2351.
- [48] J. THOMANN AND G. EICHFELDER, *A trust-region algorithm for heterogeneous multiobjective optimization*, SIAM J. Optim., 29 (2019), pp. 1017–1047.
- [49] S. TIMOSHENKO AND D. YOUNG, *Engineering Mechanics [by] S. Timoshenko [and] D.H. Young*, McGraw-Hill, 1956.
- [50] V. TORCZON, *On the convergence of pattern search algorithms*, SIAM Journal on optimization, 7 (1997), pp. 1–25.
- [51] S. WERNITZ, B. HOFMEISTER, C. JONSCHER, T. GRIESSMANN, AND R. ROLFES, *A new open-database benchmark structure for vibration-based structural health monitoring*, Structural Control and Health Monitoring, 29 (2022), p. e3077.
- [52] M. WOLNIAK, B. HOFMEISTER, C. JONSCHER, M. FANKHÄNEL, A. LOOSE, C. HÜBLER, AND R. ROLFES, *Validation of an FE model updating procedure for damage assessment using a modular laboratory experiment with a reversible damage mechanism*, Journal of Civil Structural Health Monitoring, 2190-5479 (2023).
- [53] J. J. YE, *The exact penalty principle*, Nonlinear Anal., 75 (2012), pp. 1642–1654.

CHRISTIAN GÜNTHER, LEIBNIZ UNIVERSITÄT HANNOVER, INSTITUTE OF APPLIED MATHEMATICS,
WELFENGARTEN 1, 30167 HANNOVER, GERMANY

Email address: c.guenther@ifam.uni-hannover.de

URL: ifam.uni-hannover.de/de/cguenther

BENEDIKT HOFMEISTER, LEIBNIZ UNIVERSITÄT HANNOVER, INSTITUTE OF STRUCTURAL ANALYSIS,
APPELSTRASSE 9A, 30167, HANNOVER, GERMANY

Email address: b.hofmeister@isd.uni-hannover.de

URL: <https://www.isd.uni-hannover.de/de/hofmeister>

CLEMENS HÜBLER, TU DARMSTADT, INSTITUTE OF STRUCTURAL MECHANICS AND DESIGN, FRAN-
ZISKA-BRAUN-STRASSE 3, 64287, DARMSTADT, GERMANY

Email address: huebler@ismd.tu-darmstadt.de

URL: https://www.ismd.tu-darmstadt.de/das_institut_ismd/mitarbeiter_innen_ismd/team_ismd_details_130944.de.jsp

CLEMENS JONSCHER, LEIBNIZ UNIVERSITÄT HANNOVER, INSTITUTE OF STRUCTURAL ANALYSIS, AP-
PELSTRASSE 9A, 30167, HANNOVER, GERMANY

Email address: c.jonscher@isd.uni-hannover.de

URL: <https://www.isd.uni-hannover.de/de/jonscher>

JASPER RAGNITZ, LEIBNIZ UNIVERSITÄT HANNOVER, INSTITUTE OF STRUCTURAL ANALYSIS, APPEL-
STRASSE 9A, 30167, HANNOVER, GERMANY

Email address: j.ragnitz@isd.uni-hannover.de

URL: <https://www.isd.uni-hannover.de/de/institut/personenverzeichnis/jasper-ragnitz-msc>

JENNY SCHUBERT, LEIBNIZ UNIVERSITÄT HANNOVER, INSTITUTE OF APPLIED MATHEMATICS, WEL-
FENGARTEN 1, 30167 HANNOVER, GERMANY

Email address: schubert@ifam.uni-hannover.de

URL: ifam.uni-hannover.de/schubert

MARC C. STEINBACH, LEIBNIZ UNIVERSITÄT HANNOVER, INSTITUTE OF APPLIED MATHEMATICS,
WELFENGARTEN 1, 30167 HANNOVER, GERMANY

Email address: mcs@ifam.uni-hannover.de

URL: ifam.uni-hannover.de/mcs